A LRRK2-dependent EndophilinA phosphoswitch is critical for macroautophagy at presynaptic terminals

Sandra-Fausia Soukup[1,2], Sabine Kuenen[1,2], Roeland Vanhauwaert[1,2], Julia Manetsberger[1,2], Sergio Hernández-Díaz[1,2], Jef Swerts[1,2], Nils Schoovaerts[1,2], Sven Vilain[1,2], Natalia V. Gounko[1,2], Katlijn Vints [1,2], Ann Geens[1,2], Bart De Strooper[1,2] and Patrik Verstreken[1,2,#]

[1]VIB Center for Brain & Disease Research

[2]KU Leuven, Department for Human Genetics

Leuven Institute for Neurodegenerative Disease (LIND)

3000 Leuven, Belgium

[#]e-mail: patrik.verstreken@cme.vib-kuleuven.be

Lead contact: Patrik Verstreken: patrik.verstreken@cme.vib-kuleuven.be

Synapses are often far from the soma and independently cope with proteopathic stress induced by intense neuronal activity. However, how presynaptic compartments turn-over proteins is poorly understood. We show that the synapse-enriched protein EndophilinA, thus far studied for its role in endocytosis, induces macroautophagy at presynaptic terminals. We find that EndophilinA executes this unexpected function at least partly independent of its role in synaptic vesicle endocytosis. EndophilinA-induced macroautophagy is activated when the kinase LRRK2 phosphorylates the EndophilinA-BAR domain and is blocked in animals where EndophilinA cannot be phosphorylated. EndophilinA-phosphorylation promotes the formation of highly curved membranes and reconstitution experiments show these curved membranes serve as docking stations for autophagic factors, including Atg3. Functionally, deregulation of the EndophilinA phosphorylation state accelerates activity-induced neurodegeneration. Given that EndophilinA is connected to at least three Parkinson's disease genes (LRRK2, Parkin and Synaptojanin), dysfunction of EndophilinA-dependent synaptic macroautophagy may be common in this disorder.

INTRODUCTION

Neurons can be metabolically very active, firing at rates of more than 100 Hz. Synaptic proteins and organelles are used and re-used multiple times and accumulate damage as a result of this stress. Furthermore, synapses are often located far away from the cell body and must therefore in part operate independently. This raises the question how synapses maintain protein quality. Given that neurodegeneration is thought to start with subtle synaptic defects before evolving into blunt neuronal death (Burke and O'Malley, 2013; Soukup et al., 2013), the mechanisms of synaptic protein homeostasis are likely relevant for the understanding of neurodegenerative disease.

Macroautophagy is well-placed to mediate protein turnover, but how the needs of synapses are served by this process has not been well-studied. Cellular signals like stress and amino acid deprivation induce macroautophagy, where cytoplasm is engulfed by double membrane structures before fusion with degradative lysosomes (Mizushima et al., 2011). Autophagosomes have been visualized using fluorescent markers in yeast, *Drosophila* and mammalian cells and are often observed as Atg8/LC3 positive puncta (Kabeya et al., 2000; Scott et al., 2004). At the stage of initiation, Atg9-positive vesicles fuse into elongated preautophagosomal structures with growing edges (He et al., 2006). These edges are highly curved and harbor lipid packing defects. These edges serve as protein docking sites, attracting specific autophagic factors such as Atg3, Atg14/Barkor and Atg1 that insert into such zones, recognizing specific lipids (phosphatidylinositol-3-phosphate (PI(3)P)) and lipid packing defects (Fan et al., 2011; Nath et al., 2014; Ragusa et al., 2012). The recruitment of these factors then promotes the further steps of autophagosome formation; in particular the E2-like protein Atg3 itself recruits the autophagic marker LC3/Atg8 (Nath et al., 2014). However, how these highly curved edges are formed and maintained is very poorly understood.

While autophagy has been mostly analyzed in the soma of cultured cells and yeast, autophagic markers have also been observed away from the soma at neuronal synapses

(Hernandez et al., 2012; Maday and Holzbaur, 2014; Williamson et al., 2010) and these markers were shown to be transported along axons (Maday and Holzbaur, 2014). However, how autophagosomes are formed at synapses and how the process is regulated locally at the nerve terminal is not known. We find that the presynapse-enriched protein EndophilinA (EndoA) (Ringstad et al., 1999) is present on preautophagosomal membranes and essential for autophagosome formation at presynaptic terminals. EndoA has been very well-studied for its role in synaptic vesicle endocytosis (Farsad et al., 2001; Gallop et al., 2006; Milosevic et al., 2011; Verstreken et al., 2002); and we now show that the function of EndoA in macroautophagy at synapses is direct and at least in part independent from its role in endocytosis.

Furthermore, we show that EndoA-dependent autophagy requires LRRK/LRRK2, a kinase that has also been implicated in macroautophagy in cells (Plowey et al., 2008; Tong et al., 2010). LRRK/LRRK2 phosphorylates the BAR domain of EndoA at Serine 75 (Arranz et al., 2015; Matta et al., 2012) and switches the function of the protein; non-phosphorylated EndoA tubulates membranes, while phosphorylated EndoA creates zones of very highly curved membrane and/or short tubules (Ambroso et al., 2014). Using *in vitro* and *in vivo* work, we show that these EndoA-induced highly curved membrane zones, but not EndoA-induced tubules, serve as docking sites for the autophagic factor Atg3 that drives autophagosome formation forward. While defects in autophagy have been implicated in a wide variety of diseases, we suggest that regulatory mechanisms enriched in specific cellular compartments are in place to control autophagy. Moreover, the balance of EndophilinA phosphorylation at S75 is critical for neuronal survival. In this context, the function of EndophilinA might be important in neurodegenerative disease since LRRK2 is the most commonly mutated protein in Parkinson's disease (PD) (Paisán-Ruíz et al., 2004). Furthermore, EndoA also directly interacts with Parkin and Synaptojanin, two other proteins

that are also mutated in PD (Cao et al., 2014; Krebs et al., 2013; Quadri et al., 2013; Trempe et al., 2009).

RESULTS

Metabolic and neuronal stimulation induce the formation of autophagosomes at synapses

To monitor macroautophagy at neuromuscular junctions (NMJs) we overexpressed Atg8::mCherry ($Atg8^{mCherry}$) in motor neurons (*D42-Gal4*) (**Figure S1A**). During starvation cytosolic Atg8 converts into an autophagosome-membrane-bound form (Kabeya et al., 2000). Given that macroautophagy is triggered upon starvation (Scott et al., 2004), we starved larvae for 3 h prior to dissection and live imaging. Under control conditions (fed), $Atg8^{mCherry}$ localizes in the presynaptic cytoplasmic region **(Figure 1A, A', C**, magenta**)**, but after starvation, boutonic $Atg8^{mCherry}$ becomes concentrated in puncta at presynaptic nerve endings **(Figure 1B, B',** green/blue, arrows**)**. Unbiased blind quantification of the number of puncta per area indicates an increase upon starvation **(Figure 1C**, magenta**)**. $Atg8^{mCherry}$ marks synaptic autophagosomes because when we block autophagy by knocking down Atg3, $Atg8^{mCherry}$ does not concentrate in puncta (**Figure S1B-B''**). The results are also not caused by an $Atg8^{mCherry}$-overexpression artifact, because a genomic $Atg8^{mCherry}$ transgene expressing $Atg8^{mCherry}$ at endogenous levels (**Figure S1A**), results in a very similar number of synaptic autophagosomes upon starvation **(Figure 1C**, green**)**. Furthermore, co-expression of $Atg8^{mCherry}$ with the preautophagosomal marker $Atg9^{GFP}$ indicates $Atg9^{GFP}$ rarely concentrates on Atg8 positive puncta **(Figure S1C-D**, arrows**)**. This is expected as Atg9 is recycled away before completion of the autophagosome (Orsi et al., 2012; Puri et al., 2013). Thus, macroautophagy is induced locally at the presynaptic terminals of *Drosophila* NMJs upon starvation.

Late stage Atg8^{mCherry} autophagosomes mature into organelles that are Lamp1 positive (Juhász et al., 2008). We overexpressed GFP::Lamp1 (Lamp^{GFP}), a lysosomal targeted GFP based on human Lamp1 (Pulipparacharuvil et al., 2005). When overexpressed in motor neurons, Lamp^{GFP} is present at NMJ boutons **(Figure 1D-D')**. Upon starvation, Lamp^{GFP} concentrates in puncta and it is upregulated compared to the fed condition **(Figure 1E-F)**. Similarly, labeling endogenous Lamp using anti-Lamp antibodies (Rusten et al., 2006) in starved animals indicates a similar increase in the number of dots as seen upon overexpression of Lamp^{GFP} (**Figure S1F**). Hence, Atg8^{mCherry} and Lamp^{GFP} are induced at synapses upon starvation.

We reasoned that prolonged neuronal activity might induce autophagy as a mechanism to cope with stress at synapses. We induced action potentials by overexpressing the temperature sensitive transient receptor potential cation channel A1 (TrpA1) in motor neurons and shifted the animals to 30°C (Pulver et al., 2009). 20-30 min at 30°C induces the formation of Atg8^{mCherry} positive autophagosomes (**Figure 1G',G'',** arrows) and induces the Lamp^{GFP} marker in animals expressing TrpA1, but not in control animals without TrpA1 **(Figure 1G-J'')**. We also used direct electrical motor neuron stimulation using a suction electrode. Physiologically NMJs are stimulated in bouts at <42 Hz (Titlow et al., 2014). Therefore, we challenged synapses by using a continuous 20 min 20 Hz stimulation paradigm. Again, these conditions induce macroautophagy at synaptic boutons **(Figure 1K-K'')**. Given that in these experiments the motor nerves are severed, our data indicate that our stimulation and starvation conditions reveal the local production of autophagosomes at synapses. Together, our results indicate that both starvation and in particular neuronal stimulation induce the formation of autophagosomes at presynaptic terminals.

Correlative light and electron microscopy reveals the ultrastructural nature of synaptic autophagosomes

To visualize the ultrastructural morphology of Atg8 puncta at synapses we employed transmission electron microscopy. However, Atg8^{mCherry} positive puncta at NMJ synaptic boutons are rare, even after induction of autophagy (about one in five boutons) and it would be difficult to identify these structures when 'randomly' imaging ultrathin sections of boutons. We therefore resorted to correlative light and electron microscopy that allows us to correlate Atg8 signals one-to-one to electron micrographs (Bishop et al., 2011; Urwyler et al., 2015). Animals overexpressing or endogenously expressing Atg8^{mCherry} were starved, briefly fixed and mCherry fluorescence at boutons was imaged. To identify the imaged location at the level of TEM, we burned marks in the surrounding tissue using a near-IR laser (**Figure 2B,C**). Following embedding of the sample, we used the burn marks as a guide to cut serial sections of the region. As indicated in **Figure 2D,E**, the Atg8^{mCherry} fluorescence overlays well with the presynaptic zones of the boutons within the region of interest. We then analyzed serial sections of bouton 1 (z-planes indicated in the figure), overlaying the fluorescence image with the TEM micrograph, allowing us to unequivocally identify the Atg8^{mCherry} positive puncta (**Figure 2F-I**). We repeated this procedure also using the mitochondrial marker mito-GFP that further helped with identifying Atg8^{mCherry} positive puncta (**Figure 2J**). We find a broad spectrum of morphologically distinct structures that in light microscopy were all Atg8^{mCherry} positive (**Figure 2L**). The profiles found upon overexpression of Atg8^{mCherry} or upon endogenous expression of Atg8^{mCherry} appear very similar (**Figure 2K, L'4'** and data not shown). Our work reveals that Atg8 labels an extensive spectrum of profiles at synaptic boutons.

Phosphomimetic EndoA recruits Atg3 to membranes *in vitro*

Autophagosome formation requires extensive membrane remodeling. The curved edges on nascent preautophagosomes and PI(3)P are docking sites for essential autophagic factors, including Atg3 (Fan et al., 2011; Nath et al., 2014). EndoA, a protein mostly studied for its role in synaptic vesicle endocytosis (Verstreken et al., 2002), may be a good candidate

to be involved in this process because the phosphorylation of EndoA by LRRK/LRRK2 at S75 in helix H1 alters the ability of EndoA to interact with membranes (Ambroso et al., 2014; Matta et al., 2012). Helix H1 inserts deep into the lipid bilayer, causing shallow membrane curvature and the formation of tubules on *in vitro* membranes. By contrast, when EndoA is phosphorylated, the protein inserts less deep into the lipid bilayer, causing increased curvature by wedging Helix H1 into the lipid head group region (Ambroso et al., 2014). Confirming this model, phosphodead EndoA^{S75A} (or non-phosphorylated wild type EndoA) mostly forms long tubules from PI(3)P-containing giant unilamellar vesicle (GUV) membranes **(Figure S2A-C'** arrows and **E**, (Matta et al., 2012)**)**. In contrast, phosphomimetic EndoA^{S75D} does not form long tubules, but mostly induces much shorter tubules or narrow membrane bends **(Figure S2D,D'** arrowheads and **E)**. Moreover, phosphorylation of EndoA switches the activity of the protein (Ambroso et al., 2014).

To determine if EndoA^{S75D} promotes Atg3-recruitment to membranes *in vitro*, we incubated PI(3)P-containing GUVs with purified Atg3::mCherry and purified EndoA^{S75D} or EndoA^{S75A}. Atg3::mCherry is recruited to membrane patches with short tubules and bends on GUVs incubated with EndoA^{S75D} **(Figure 3A-C'')**. In contrast, only little Atg3::mCherry is recruited to GUVs incubated with EndoA^{S75A} **(Figure 3D-D'')** and also not to the long EndoA^{S75A}-induced tubular membrane areas **(Figure 3E-E'')**. Blind quantification of the amount of Atg3 membrane recruitment indicates a strong preference of Atg3 to associate with PI(3)P-containing GUV membranes incubated with EndoA^{S75D} **(Figure 3F)**. Given that EndoA is a presynapse-enriched protein (Dickman et al., 2015; Guichet et al., 2002; Verstreken et al., 2002), our data predict that EndoA acts in macroautophagy at synaptic terminals.

EndoA is required for autophagy at presynaptic terminals

We assessed the localization of EndoA at synapses upon starvation to induce autophagy. Like the preautophagosomal markers Atg9^{GFP}, Atg6^{myc} (Juhász et al., 2008) or

Atg16^{GFP}, EndoA distributes broadly **(Figure 4A-A'')** and data not shown). Next, we immunoprecipitated neuronally overexpressed Atg9, the only transmembrane protein in autophagy (Young et al., 2006), and probed for EndoA. We used flies that also overexpress LRRK2^{G2019S}, a condition that induces autophagy in neurons (see below). Interestingly, in Atg9^{GFP}-immunoprecipitates from adult fly head extracts we detect EndoA **(Figure 4B)**, suggesting the protein is present on preautophagosomal membranes *in vivo*.

endoA null mutants display morphological defects at synapses, grow slow, show strong chronic endocytic defects and few animals survive (Dickman et al., 2015; Guichet et al., 2002; Verstreken et al., 2002). To circumvent these issues, we used a conditional approach: FlAsH Assisted Light Inactivation (FlAsH-FALI; Kasprowicz et al., 2014; Marek and Davis, 2002). Here, a tetracysteine-tag (4C) is fused to EndoA (EndoA^{4C}). The 4C tag tightly binds FlAsH, an exogenously added compound, that when excited at 405 nm, acutely inactivates the tagged protein within seconds. Estimates indicate that the half-maximal inactivation distance of FALI is approximately 30-40 Å, well within the range of single proteins (Beck et al., 2002). We expressed EndoA^{4C} at endogenous levels in *endoA*$^{-/+}$ mutants and show EndoA^{4C} is a functional protein because these animals survive and they show FM 1-43 dye uptake into newly endocytosed synaptic vesicles, similar to wild type controls (not shown and Kasprowicz et al., 2014). We then loaded EndoA^{4C} with FlAsH and used light to inactivate the protein locally **(Figure 4C)**. Boutons become rapidly devoid of EndoA function as much less FM 1-43 dye is internalized upon stimulation **(Figure 4D)**. The defect in dye uptake after light inactivation is similar to that observed in *endoA* null mutants (Dickman et al., 2015; Guichet et al., 2002; Verstreken et al., 2002), but different from that observed upon acute inactivation of other proteins involved in endocytosis, including Clathrin heavy and light chain and Dynamin (Heerssen et al., 2008; Kasprowicz et al., 2014), indicating specificity of the approach.

We then assessed autophagosome formation (using Atg8^{mCherry}) after 30 min of 20 Hz nerve stimulation. Atg8^{mCherry} dots form normally in stimulated non-EndoA^{4C}-expressing controls with FlAsH treatment and with or without light (+FlAsH, +/-light). Quantification of Atg8^{mCherry} dots in EndoA^{4C}-expressing animals indicates that inactivation of EndoA (+FlAsH, +light), prior to nerve stimulation, interferes with the formation of autophagosomes **(Figure 4E-E'''**). Hence, EndoA is required to induce macroautophagy at synaptic boutons upon neuronal stimulation.

Previous work in cultured cells indicated a chronic requirement of endocytosis for macroautophagy by mediating the trafficking of Atg9 and other factors (Dwivedi et al., 2011; Puri et al., 2013). Whether endocytosis is also acutely needed during the formation of an autophagosome, is not known. We therefore turned to the temperature sensitive *dynamin* mutants (*shi^{ts1}*). These mutants lose synaptic vesicle endocytosis as Dynamin function is blocked within seconds at restrictive temperatures (>30°C) (Verstreken et al., 2002). In contrast to our observations upon acute inactivation of EndoA, Atg8^{mCherry} puncta form normally after starvation at *shi^{ts1}* synapses kept at restrictive temperature (37 °C) (**Figure 4F-H**). Hence, our results indicate that an acute block in endocytosis *per se* does not significantly affect autophagosome formation at synapses and they reveal that EndoA plays a role at least in part independent from its function in synaptic vesicle endocytosis.

Phosphorylation of EndoA is a switch for autophagy at presynaptic terminals

To test if macroautophagy at synapses depends on the Serine 75 phosphorylation status of EndoA, we overexpressed Atg8^{mCherry} or Lamp^{GFP} in *endoA* null mutant flies that express at endogenous levels phosphodead EndoA^{S75A} or phosphomimic EndoA^{S75D} (Matta et al., 2012). Animals expressing EndoA^{S75A} fail to induce autophagy at synapses when starved (**Figure 5A-A', D** and **S3A-A', D**), while animals expressing EndoA^{S75D} already induce synaptic autophagy under fed conditions (**Figure 5B-B', D** and **S3B-B', D**). The defects are rescued in *endoA$^{-/-}$* null mutant animals that express wild type EndoA at endogenous levels

(Figure 5C-D and **S3C-D)**. Hence, our data suggest that phosphorylation of EndoA at Serine 75 is necessary to induce autophagy at synapses.

We next assured ourselves that autophagosomes at synapses in EndoA^{S75A} animals are not lower in number because they are transported or degraded faster than in controls. First, the number of Atg8^{mCherry} puncta in axons of EndoA^{S75A} expressing animals is not increased compared to controls (data not shown). Second, we blocked autophagic flux with Chloroquine that inhibits autophagosome-to-lysosome fusion. In controls this results in an increased number of Atg8^{mCherry} positive puncta at synapses, but EndoA^{S75A} expressing animals still fail to form Atg8^{mCherry} positive puncta (fed or starved) **(Figure S3E-H)**. Hence, synaptic autophagosome formation, not transport or degradation is affected by EndoA.

The defect in macroautophagy in EndoA phosphomutants does not appear to be explained by a defect in endocytosis. While both EndoA^{S75D} and EndoA^{S75A} show mild defects in endocytosis (Matta et al., 2012), EndoA^{S75A}-expressing animals show less synaptic macroautophagy and EndoA^{S75D}-expressing animals more. Hence, the mild endocytic defects in these animals do not correlate with the synaptic autophagy defects we report. In addition, we also do not observe obvious differences of Atg9^{GFP} distribution at synapses of EndoA^{S75A} or EndoA^{S75D} animals compared to wild type controls **(Figure S3 I-K')**. We conclude that the localization of the preautophagosomal marker Atg9 that is dependent on endosomal trafficking (Puri et al., 2013), is not noticeably altered by the mild endocytic defects seen in the EndoA phosphomutants.

Next we tested if the phosphorylation status of EndoA affects Atg3 localization. We created *endoA*$^{-/-}$ null mutant animals that express EndoA^{S75A} or EndoA^{S75D} at endogenous levels and simultaneously also overexpress Atg3^{HA} **(Figure S1E)** and Atg8^{mCherry}. While both Atg3^{HA} and Atg8^{mCherry} are broadly distributed in boutons of fed larvae **(Figure 5E-E'')**, when control animals are starved, both markers concentrate in puncta **(Figure 5F-F'',** arrows**)**

and significantly overlap **(**Pearson correlation within the mask of Atg8^{mCherry}, **Figure 5K).** In contrast, Atg8^{mCherry} and Atg3^{HA} do not concentrate in puncta in fed or starved EndoA^{S75A} expressing animals **(Figure 5G-H'')** and the markers colocalize much less **(Figure 5K).** In EndoA^{S75D} animals Atg3^{HA} and Atg8^{mCherry} again concentrate in puncta and colocalize **(Figure 5I- K,** arrows**)**. These data are consistent with our *in vitro* results and they suggest EndoA^{S75D} creates docking sites for Atg3 at synapses.

LRRK kinase function regulates EndoA-induced macroautophagy at synaptic boutons

We previously showed that LRRK and its mammalian homologue LRRK2 phosphorylate EndoA/EndoA1 (Arranz et al., 2015; Matta et al., 2012), suggesting that EndoA-dependent macroautophagy at synapses is dependent on LRRK activity. We therefore expect (1) LRRK and EndoA to be both present at presynaptic terminals; (2) *lrrk* null mutants to block macroautophagy and (3) overexpression of the kinase active LRRK2^{G2019S} mutant to enhance the process. Using a *LRRK-HA* knock-in allele (Vilain et al., 2014) we demonstrate that similar to EndoA, LRRK is enriched at presynaptic terminals **(Figure 6A-A'' and S4A-E)**. We then overexpressed Atg8^{mCherry} or Lamp^{GFP} in *lrrk*$^{-/-}$ mutants and find that neither Atg8^{mCherry} nor Lamp^{GFP} are induced after starvation **(Figure 6B-C',F and S5A-B',E).** Similarly, when we use the heat sensitive channel TrpA1 at 30°C to induce action potentials in *lrrk*$^{-/-}$ mutant motor neurons, autophagy measured using Atg8^{mCherry} and Lamp^{GFP} markers, is not induced **(Figure 6G-I** and **S5F-H)**. Expression of wild type LRRK at endogenous levels as well as overexpression of human LRRK2^{WT} (*D42-Gal4*) rescue the autophagy defect of *lrrk*$^{-/-}$ mutants **(Figure 6D-F** and **S5C-E)**. Hence, similar to EndoA, LRRK is required to induce macroautophagy at the synapse.

Next, we tested if the kinase activity of LRRK2 is sufficient to induce autophagy at synapses. Overexpression of LRRK2^{G2019S} (*D42-Gal4*) induces the Atg8^{mCherry} and Lamp^{GFP} markers at boutons also under fed conditions **(Figure 6J-J',L** and **S5I,I',K)**. In contrast,

overexpression of the kinase dead LRRK2^{D2017A} (*D42-Gal4*) in a wild type background does not induce the Atg8^{mCherry} and Lamp^{GFP} markers under fed conditions **(Figure 6K,L** and **S5J,K)**. This indicates the effect is not the mere result of overexpression but caused by increased kinase activity. Note that under starvation, animals overexpressing LRRK2^{D2017A} still support synaptic autophagy **(Figure 6K-L** and **S5J-K)**, because wild type fly LRRK is still present. These data indicate that the kinase activity of LRRK2 induces autophagy at synapses.

To further scrutinize the relationship between LRRK and EndoA we used genetic interactions. While *lrrk*$^{-/-}$ blocks the induction of autophagy, adding a copy of EndoA^{S75D} induces the process again, even under fed conditions **(Figure 7A,A',D** and **S6A-B',E)**. As expected, adding a copy of EndoA^{S75A} does not induce these autophagic markers **(Figure 7B,B',D** and **S6C,C',E)**. Furthermore, LRRK2^{G2019S} induces the autophagic markers under starved and fed conditions **(Figure 6J,J',L** and **S5I,I',K)**, but this effect is lost when endogenous *endoA* is replaced by *endoA*^{S75A} (*endoA*^{S75A}*;endoA*$^{-/-}$ *D42>LRRK2*^{G2019S}) **(Figure 7C-D** and **S6D-E)**. These results further indicate that EndoA acts downstream of LRRK and suggest that LRRK-dependent phosphorylation of EndoA at Serine 75 promotes macroautophagy at synapses.

The balance of EndoA phosphorylation affects neuronal survival

To test if EndoA is connected to neurodegeneration (a hallmark of PD) we assessed neuronal function and cellular integrity of flies reared in constant light to stimulate the retina. We removed EndoA only in the eye (*eyFLP*, Newsome et al., 2000), circumventing lethality and evaluated neuronal function using electroretinograms (ERGs). ERGs measure the ability of photoreceptors to depolarize in response to a light pulse. In contrast to controls, flies with *endoA*$^{-/-}$ mutant eyes show a progressive decline in the ability of the photoreceptors to depolarize (green bar, **Figure 8A-B', G**). When the retina is not continuously stimulated by rearing flies in the dark, we do not observe such defects **(Figure 8A,B, G)**. This phenotype is

often connected to photoreceptor cell degeneration (Soukup et al., 2013). Using TEM, we confirm the degeneration of light-stimulated *endoA* mutant photoreceptor cell bodies and synaptic terminals in the lamina **(Figure S7A)**. Quantification compared to controls indicates a lower number of photoreceptor cell bodies per ommatidia as well as degenerating photoreceptor synaptic terminals per cartridge in 7 day light-stimulated *endoA*$^{-/-}$ mutant eyes **(Figure 8C-F,H,I)**, but not in dark reared flies **(Figure S7B,C,I,J)**. Hence, these data indicate an important role for EndoA to prevent activity dependent neurodegeneration in flies.

To test if the phosphorylation status of EndoA affects neuronal survival we examined *endoA*$^{-/-}$ flies expressing either EndoA^{S75A} or EndoA^{S75D} as well as *lrrk*$^{-/-}$ mutants. The red eye pigment in these flies was genetically removed (using *cn, bw* mutations) as it interferes with the degeneration progress. *endoA* mutant flies expressing EndoA^{S75A} or EndoA^{S75D} and *lrrk*$^{-/-}$ mutants, reared in constant light, show a progressive decrease in the ability of the photoreceptors to depolarize **(Figure 8J-L',S and S7G,G').** In contrast, control flies (*cn bw*) reared in constant light show only a mild reduction in the depolarization of ERG recordings **(Figure 8J,J',S).** Also the number of photoreceptor cell bodies per ommatidium and the number of photoreceptor terminals per cartridge are significantly lower in *endoA*$^{-/-}$ animals expressing EndoA^{S75A} or EndoA^{S75D} and in *lrrk*$^{-/-}$ mutant flies reared in light compared to controls **(Figure 8M-R,T,U and S7H',N')**. Again rearing the flies for seven days in the dark does not result in degeneration of photoreceptors **(Figure S7D-F, H, K-N).**

We tested if EndoA phosphomutants also affect dopaminergic neuron survival, since in PD dopaminergic neurons degenerate. We aged *endoA*$^{-/-}$ mutant flies that express EndoA^{S75A} or EndoA^{S75D} for 30 days. Both genotypes, compared to controls, reveal a lower number of TH-positive cells in the "PPM3 and PPL1" dopaminergic neuron clusters (**Figure S8A-C**). Hence, we find that both EndoA^{S75A} as well as EndoA^{S75D} cause neurodegeneration, suggesting a correct balance of EndoA phosphorylation is required for neuronal survival.

DISCUSSION

In this work, we provide evidence for an unexpected function of EndoA in the induction of macroautophagy at presynaptic terminals. During neuronal activity and metabolic stress, autophagy may serve the special needs of the synapse in protein turnover. EndoA is a presynapse-enriched protein that had only been studied for its role in endocytosis; we now show that phosphorylated EndoA also directly acts in autophagosome formation at synapses. The balance of EndoA phosphorylation at S75 is not only critical for autophagy, but also for neuronal survival. Similarly, EndoA knock-out mice suffer from neurodegeneration (Milosevic et al., 2011); indicating evolutionary conservation. The current finding also provides a conceptual framework to investigate why abnormal protein folding and aggregation, underlying many neurodegenerative disorders, affect the normal functioning of synapses at early stages of these diseases and it will be interesting to investigate macroautophagy at synapses in the context of specific neurodegenerative conditions including PD.

EndoA interacts via its SH3 domain with Dynamin and Synaptojanin (Ringstad et al., 1999). These and other data strongly implicate EndoA in synaptic vesicle endocytosis (Milosevic et al., 2011; Schuske et al., 2003; Verstreken et al., 2002). The proper localization of preautophagic components in the cell has previously been shown to dependent on a chronic need for endocytosis (Dwivedi et al., 2011; Puri et al., 2013). Hence, by virtue of its role in endocytosis, EndoA could affect autophagy.

Here, we provide several lines of evidence that EndoA, in addition to its role in endocytosis, also acts directly in macroautophagy at synapses: First, both EndoA^{S75A} and EndoA^{S75D} display only mild endocytic defects (Matta et al., 2012), yet EndoA^{S75A} blocks synaptic macroautophagy and EndoA^{S75D} promotes it. Second, Atg9 localization is dependent on proper endocytosis but Atg9 localization is not obviously altered in EndoA phosphomutants. Third, EndoA localizes on preautophagosomal membranes. Finally, acute

inhibition of Dynamin using *shi*^{ts1} mutants blocks endocytosis but not autophagosome formation, in contrast to acute inactivation of EndoA. Hence, the acute block of endocytosis does not block macroautophagy at synapses. Together, these data argue that EndoA acts in macroautophagy at synapses at least in part independent from its function in synaptic vesicle endocytosis. Our work is not contradicting previous findings that indicate endocytosis is needed to localize preautophagosomal components (Dwivedi et al., 2011; Puri et al., 2013). Indeed, the conditions we applied: the acute inactivation of endocytosis using *shi*^{ts1} or the mild (chronic) endocytic defects in EndoA phosphomutants, appear insufficient to affect this maturation process.

EndoA comprises an N-terminal BAR domain that it uses to induce, stabilize or sense membrane curvature (Farsad et al., 2001; Gallop et al., 2006). Previous work showed that LRRK2 phosphorylates helix H1 in the EndoA BAR domain at Serine 75, altering the protein's membrane association properties (Ambroso et al., 2014; Matta et al., 2012). Non-phosphorylated EndoA associates tighter with membranes than phosphorylated EndoA (Matta et al., 2012), and *in vitro* EndoA creates tubules, similar to several other proteins implicated in synaptic vesicle endocytosis (Farsad et al., 2001; Peter et al., 2004). In contrast, phosphorylated EndoA is pushed further away from the membrane and *in vitro* the protein creates zones of highly curved membranes or short tubules, such as those present at the edge of a growing preautophagosome (Ambroso et al., 2014; Matta et al., 2012; Ragusa et al., 2012). Hence, S75 phosphorylation in EndoA controls a switch that toggles the function of the protein between different types of membrane deformation.

While it is very challenging to locate EndoA at the preautophagosome edge *in vivo*, highly curved membrane domains serve as docking sites for autophagic factors including Atg3, Atg14 and Atg1 (Fan et al., 2011; Nath et al., 2014; Ragusa et al., 2012). We show that Atg3^{mCherry} docks on EndoA^{S75D}-induced curved GUV membranes but that much less Atg3 is recruited to GUV membranes or tubules when incubated with EndoA^{S75A}. This suggests that

Atg3 detects lipid packing defects in highly curved membranes, possibly by inserting an helix into the bent membrane (Nath et al., 2014; Lauwers et al., 2016). Also *in vivo* EndoA^{S75A} expressing animals fail to recruit Atg3 to autophagosomes. An exciting model may thus be that the phosphorylation state of EndoA defines (1) protein localization and (2) whether the protein acts during autophagy. How EndoA itself is diverted from its role in endocytosis to preautophagosomal membranes and what other autophagic factors are recruited by EndoA remains to be defined.

The concept of synaptic dysfunction and proteopathic stress as a consequence of failing protein quality control in neurodegenerative disease is emerging, but how quality control systems operate at synapses is poorly understood. Macroautophagy turns over proteins and defects in autophagy connect to neurodegeneration, also PD (Komatsu et al., 2006). Macroautophagy mutants *atg5* and *atg7* display neurodegeneration and both genes are risk factors in PD (Chen et al., 2013a, 2013b; Hara et al., 2006; Juhász et al., 2007; Komatsu et al., 2006).

PD is often characterized by misfolded, dysfunctional proteins and synaptic dysfunction is recognized in PD models as well (Burke and O'Malley, 2013). Consistently, autophagic defects are observed in patient-derived cells and in PD cellular- and animal-models, including LRRK2 models (Plowey et al., 2008; Tong et al., 2010). Macroautophagic markers are also present at presynaptic terminals (Hernandez et al., 2012; Maday and Holzbaur, 2014); but neither the regulatory mechanisms of synaptic autophagosome formation, nor a role for EndoA in this process have been investigated. We now connect LRRK2 to the induction of autophagy at synapses and show kinase activity towards EndoA is critical. A correct balance of LRRK2 activity may be relevant to familial PD caused by mutations in *LRRK2*. While *LRRK2*^{G2019S} carriers are expected to harbor increased kinase activity, not all *LRRK2* pathogenic mutations result in increased kinase activity. The central role of EndoA in autophagy may be a common pathway in PD because EndoA also binds to

Parkin and Synaptojanin, two other proteins linked to PD (Cao et al., 2014; Krebs et al., 2013; Quadri et al., 2013; Trempe et al., 2009). Hence, a network of PD-relevant factors emerges that regulates EndoA and thus likely also autophagy at synapses. The phosphorylation state of EndoA might therefore be a nexus explaining synaptic defects in PD.

The discovery of a role for EndoA phosphorylation in macroautophagy at synapses and the connection to PD is also interesting in the context of the known role for Endophilin B1/Bax-interacting factor 1 (EndoB1) in macroautophagy (Takahashi et al., 2011; Wong et al., 2011). EndoB1 also contains an N-BAR domain, but the protein is not phosphorylated by LRRK2 (Arranz et al., 2015) and it is not known if EndoB1 acts at synapses. Interestingly, EndoB1 is connected to PD as well. Cdk5 phosphorylates EndoB1 at T145 and this induces autophagy (Wong et al., 2011). Cdk5 activity in turn is induced by PD models including MPTP, a mitochondrial toxin, or by pathogenic alpha-synuclein^{A53T}. Hence, EndoA and EndoB can both induce macroautophagy, but the mechanisms must be different because EndoB does not compensate for the loss of EndoA. Nevertheless, it is exciting that both events are connected to PD and it will be interesting to address if EndoB1, like EndoA, also acts at synapses.

Our work demonstrates the existence of a protein quality control system at the level of the synapse regulated by EndoA that maintains the health of the synapse, especially under intense stimulation. We propose that deregulation of this mechanism progressively leads to synaptic dysfunction and connects to PD. However, how autophagy defects result in neuronal demise needs further investigation. Specifically at the synapse, the role of EndoA tightly couples the major function of the presynapse (neurotransmission) with this quality control and disposal system.

AUTHOR CONTRIBUTIONS

SFS and PV conceived the study, SFS, PV and BDS analyzed data and wrote the paper. JM developed the CLEM protocol and SFS, SK, RV, JM, SH-D, JF, SV, KV, NVG and PV performed experiments and/or provided reagents.

ACKNOWLEDGMENTS

We thank T. Neufeld, H. Krämer, G. Juhász, H. Stenmark, the Bloomington Drosophila Stock Center, FlyORF and the DSHB for reagents, E. Lauwers and the VIB Bioimaging core Leuven for help. Support was provided by KU Leuven (CREA, GOA), ERC CoG, FWO, opening the future, the Hercules Foundation, IWT fellowship to RV, BELSPO, a Methusalem grant of the Flemish government and VIB. The authors declare no competing financial or other conflict of interest.

EXPERIMENTAL PROCEDURES

Transgenic flies and molecular biology

Flies used are listed in supplemental section.

GFP::Atg9 (*Drosophila*) was created by Gibson assembly (NEB) using two PCR products: Atg9 and GFP (supplemental methods) and cloned into the XhoI and XbaI sites of pUAST-attB that was inserted in VK20 (3R, 99F8). The *lrrk* genomic rescue construct is CH322-120O10 P[acman] (BACPAC Resources Center [BPRC]) inserted into attP-9A (VK18) (2R, 53B2). IPs were performed on Da>UAS-LRRK2^{G2019S} (control) and Da>UAS-LRRK2^{G2019S}, UAS-ATG9^{GFP} adult head extracts using GFP-Trap magnetic beads (Cromotec Inc.). Protein production of EndoA and Atg3 followed standard procedures (supplemental methods).

GUVs were prepared by electroswelling for 2 h 10 Hz and 1.2 V in 300 mM sucrose solution. GUVs contained 39.5 mol% L-a-phosphatidylcholine, 19.5 mol% L-a-phosphatidylethanolamine, 34.5 mol% L-a-phosphatidylserine, 4.5 mol% 1.2-dioleoyl-*sn*-

glycero-3-phospho-(1'-myo-inositol-3'-phosphate) (PI(3)P) (Avanti), and 2 mol% DiO (Invitrogen). GUVs were incubated with 600 nM EndoA^{WT}, EndoA^{S75A} or EndoA^{S75D} for 10 min at 30 °C, and then incubated with 400 nM Atg3::mCherry-Myc for 30 min at 30 °C. Samples were spun at 4 °C - 1400 rpm - 30 min and resuspended in 50 mM Hepes 150 mM NaCl. Resuspended GUVs were added to BSA pretreated coverslips and GUVs (600-800 nm diameter) were imaged on a Nikon A1R confocal microscope and included for quantification.

Details of immunohistochemistry are in the supplemental methods.

Autophagy assays

Autophagy by starvation: third instar larvae were placed in petri dishes with 20% sucrose and 1% agarose for 3h-4h (Scott et al., 2004). For *shi^{ts1}*, larvae were grown at 22 °C and starved for 2 h at 22 °C and then moved to a preheated 33°C tube for 1 h. Animals were then dissected in heated HL3, in mM: 110 NaCl, 5 KCl, 10 $NaHCO_3$, 5 Hepes, 30 sucrose, 5 trehalose, 10 $MgCl_2$, pH 7.2 (Stewart et al., 1994).

Autophagy by stimulation: TrpA1 (D42-Gal4) expressing larvae grown at 18 °C were placed in a preheated 30 °C tube and dissected in heated HL3. Alternatively we used a suction electrode for 30 min of direct motor nerve stimulation (20Hz) in larvae incubated in HL3 with 1 mM $CaCl_2$. 100 µM 1-Naphthylacetyl spermine trihydrochloride (Sigma) was added during imaging to prevent muscle contractions.

To study flux, fed third instar larvae were placed for 4h on standard food with 10 mg/ml Chloroquine diphosphate salt (Sigma).

Correlative light and electron microscopy and FlAsH-FALI

Boutons expressing Atg8^{mCherry} were imaged on a two-photon confocal microscope and marked by Near-infrared branding (NIRB) followed by EM processing (Bishop et al., 2011; Urwyler et al., 2015). FlAsH-FALI was performed as described (Kasprowicz et al., 2014; Marek and Davis, 2002). Both procedures are also described in the supplemental methods.

Imaging and quantification

For live imaging (also FlAsH-FALI), dissected larvae were incubated in HL3 and imaged on a Nikon A1R confocal microscope with a 60x NA1.0 water immersion lens. Fluorescence was quantified in ImageJ: $Lamp^{GFP}$ or $Atg8^{mCherry}$ intensities were calculated by applying a threshold to mark boutonic areas in a single plane followed by measuring the mean pixel intensities in these areas. The number of $Lamp1^{GFP}$ or $Atg8^{mCherry}$ puncta was measured using particle analysis of a binary image combined with applying a threshold mask on the cytoplasmic signal for the bouton area. The data was blinded before quantification.

Colocalisation of $Atg8^{mCherry}$ dots and $Atg3^{3xHA}$ dots was calculated using JACoP in ImageJ, where an object based Pearson correlation coefficient is defined by thresholding the $Atg8^{mcherry}$ puncta (thresholded overlay colocalization coefficient).

Boutonic images of $Atg8^{mCherry}$ or $Lamp1^{GFP}$ acquired with identical settings were indexed and color codified using a 16 color LUT. Figures were composed in Adobe Photoshop CS5.

Statistics

Statistical significance was determined using GraphPad Prism 6. Distribution of data was assessed using a D'Agostino-Pearson Omnibus test. Normal distributed data were tested with parametric tests: for two datasets we used a student's t-test. For more than two datasets we used a one-way analysis of variance test (ANOVA) and a post hoc Tukey test. Non-normal distributed data were tested using non-parametric tests: for two datasets we used a Mann Whitney test and for more than two datasets we used an ANOVA-Kruskal Wallis test and a Dunn's test. Significance levels used ****=$p<0.0001$, ***=$p<0.001$, **=$p<0.01$,*=$p<0.05$, ns=$p>0.05$. 'n' in the legends indicates the number of boutons or NMJs analyzed.

REFERENCES

Ambroso, M.R., Hegde, B.G., Langen, R., 2014. Endophilin A1 induces different membrane shapes using a conformational switch that is regulated by phosphorylation. Proc. Natl. Acad. Sci. U. S. A. 111, 6982–7.

Arranz, A.M., Delbroek, L., Van Kolen, K., Guimarães, M.R., Mandemakers, W., Daneels, G., Matta, S., Calafate, S., Shaban, H., Baatsen, P., De Bock, P.-J., Gevaert, K., Vanden Berghe, P., Verstreken, P., De Strooper, B., Moechars, D., 2015. LRRK2 functions in synaptic vesicle endocytosis through a kinase-dependent mechanism. J. Cell Sci. 128 , 541–552.

Beck, S., Sakurai, T., Eustace, B.K., Beste, G., Schier, R., Rudert, F., Jay, D.G., 2002. Fluorophore-assisted light inactivation: A high-throughput tool for direct target validation of proteins. Proteomics 2, 247–255.

Bishop, D., Nikic, I., Brinkoetter, M., Knecht, S., Potz, S., Kerschensteiner, M., Misgeld, T., 2011. Near-infrared branding efficiently correlates light and electron microscopy. Nat Meth 8, 568–570.

Burke, R.E., O'Malley, K., 2013. Axon degeneration in Parkinson's disease. Exp. Neurol. 246, 72–83.

Cao, M., Milosevic, I., Giovedi, S., De Camilli, P., 2014. Upregulation of Parkin in Endophilin Mutant Mice. J. Neurosci. 34, 16544–16549.

Chen, D., Pang, S., Feng, X., Huang, W., Hawley, R.G., Yan, B., 2013a. Genetic analysis of the ATG7 gene promoter in sporadic Parkinson's disease. Neurosci. Lett. 534, 193–8.

Chen, D., Zhu, C., Wang, X., Feng, X., Pang, S., Huang, W., Hawley, R.G., Yan, B., 2013b. A novel and functional variant within the ATG5 gene promoter in sporadic Parkinson's

disease. Neurosci. Lett. 538, 49–53.

Dickman, D.K., Horne, J.A., Meinertzhagen, I.A., Schwarz, T.L., 2015. A Slowed Classical Pathway Rather Than Kiss-and-Run Mediates Endocytosis at Synapses Lacking Synaptojanin and Endophilin. Cell 123, 521–533.

Dwivedi, M., Sung, H., Shen, H., Park, B.J., Lee, S., 2011. Disruption of endocytic pathway regulatory genes activates autophagy in C. elegans. Mol. Cells 31, 477–481.

Fan, W., Nassiri, a., Zhong, Q., 2011. Autophagosome targeting and membrane curvature sensing by Barkor/Atg14(L). Proc. Natl. Acad. Sci. 108, 7769–7774.

Farsad, K., Ringstad, N., Takei, K., Floyd, S.R., Rose, K., De Camilli, P., 2001. Generation of high curvature membranes mediated by direct endophilin bilayer interactions. J. Cell Biol. 155, 193–200.

Gallop, J.L., Jao, C.C., Kent, H.M., Butler, P.J.G., Evans, P.R., Langen, R., McMahon, H.T., 2006. Mechanism of endophilin N-BAR domain-mediated membrane curvature. EMBO J. 25, 2898–910.

Guichet, A., Wucherpfennig, T., Dudu, V., Etter, S., Wilsch-Bräuniger, M., Hellwig, A., González-Gaitán, M., Huttner, W.B., Schmidt, A. a, 2002. Essential role of endophilin A in synaptic vesicle budding at the Drosophila neuromuscular junction. EMBO J. 21, 1661–72.

Hara, T., Nakamura, K., Matsui, M., Yamamoto, A., Nakahara, Y., Suzuki-Migishima, R., Yokoyama, M., Mishima, K., Saito, I., Okano, H., Mizushima, N., 2006. Suppression of basal autophagy in neural cells causes neurodegenerative disease in mice. Nature 441, 885–889.

He, C., Song, H., Yorimitsu, T., Monastyrska, I., Yen, W.L., Legakis, J.E., Klionsky, D.J., 2006. Recruitment of Atg9 to the preautophagosomal structure by Atg11 is essential for

selective autophagy in budding yeast. J. Cell Biol. 175, 925–935.

Heerssen, H., Fetter, R.D., Davis, G.W., 2008. Clathrin Dependence of Synaptic-Vesicle Formation at the Drosophila Neuromuscular Junction. Curr. Biol. 18, 401–409.

Hernandez, D., Torres, C. a, Setlik, W., Cebrián, C., Mosharov, E. V, Tang, G., Cheng, H.-C., Kholodilov, N., Yarygina, O., Burke, R.E., Gershon, M., Sulzer, D., 2012. Regulation of presynaptic neurotransmission by macroautophagy. Neuron 74, 277–84.

Juhász, G., Erdi, B., Sass, M., Neufeld, T.P., 2007. Atg7-dependent autophagy promotes neuronal health, stress tolerance, and longevity but is dispensable for metamorphosis in Drosophila. Genes Dev. 21, 3061–6.

Juhász, G., Hill, J.H., Yan, Y., Sass, M., Baehrecke, E.H., Backer, J.M., Neufeld, T.P., 2008. The class III PI(3)K Vps34 promotes autophagy and endocytosis but not TOR signaling in Drosophila. J. Cell Biol. 181, 655–66.

Kabeya, Y., Mizushima, N., Ueno, T., Yamamoto, a, Kirisako, T., Noda, T., Kominami, E., Ohsumi, Y., Yoshimori, T., 2000. LC3, a mammalian homologue of yeast Apg8p, is localized in autophagosome membranes after processing. EMBO J. 19, 5720–8.

Kasprowicz, J., Kuenen, S., Swerts, J., Miskiewicz, K., Verstreken, P., 2014. Dynamin photoinactivation blocks Clathrin and α-adaptin recruitment and induces bulk membrane retrieval. J. Cell Biol. 204 , 1141–1156.

Komatsu, M., Waguri, S., Chiba, T., Murata, S., Iwata, J., Tanida, I., Ueno, T., Koike, M., Uchiyama, Y., Kominami, E., Tanaka, K., 2006. Loss of autophagy in the central nervous system causes neurodegeneration in mice. Nature 441, 880–884.

Krebs, C.E., Karkheiran, S., Powell, J.C., Cao, M., Makarov, V., Darvish, H., Di Paolo, G.,

Walker, R.H., Shahidi, G.A., Buxbaum, J.D., De Camilli, P., Yue, Z., Paisán-Ruiz, C., 2013. The Sac1 domain of SYNJ1 identified mutated in a family with early-onset progressive parkinsonism with generalized seizures. Hum. Mutat. 34, 1200–1207.

Maday, S., Holzbaur, E.L.F., 2014. Autophagosome biogenesis in primary neurons follows an ordered and spatially regulated pathway. Dev. Cell 30, 71–85.

Marek, K.W., Davis, G.W., 2002. Transgenically Encoded Protein Photoinactivation (FlAsH-FALI): Acute Inactivation of Synaptotagmin I. Neuron 36, 805–813.

Matta, S., Van Kolen, K., da Cunha, R., van den Bogaart, G., Mandemakers, W., Miskiewicz, K., De Bock, P.-J., Morais, V. a, Vilain, S., Haddad, D., Delbroek, L., Swerts, J., Chávez-Gutiérrez, L., Esposito, G., Daneels, G., Karran, E., Holt, M., Gevaert, K., Moechars, D.W., De Strooper, B., Verstreken, P., 2012. LRRK2 controls an EndoA phosphorylation cycle in synaptic endocytosis. Neuron 75, 1008–21.

Milosevic, I., Giovedi, S., Lou, X., Raimondi, A., Collesi, C., Shen, H., Paradise, S., O'Toole, E., Ferguson, S., Cremona, O., De Camilli, P., 2011. Recruitment of endophilin to clathrin-coated pit necks is required for efficient vesicle uncoating after fission. Neuron 72, 587–601.

Mizushima, N., Yoshimori, T., Ohsumi, Y., 2011. The role of Atg proteins in autophagosome formation. Annu. Rev. Cell Dev. Biol. 27, 107–32.

Nath, S., Dancourt, J., Shteyn, V., Puente, G., Fong, W.M., Nag, S., Bewersdorf, J., Yamamoto, A., Antonny, B., Melia, T.J., 2014. Lipidation of the LC3/GABARAP family of autophagy proteins relies on a membrane-curvature-sensing domain in Atg3. Nat Cell Biol 16, 415–424.

Newsome, T.P., Asling, B., Dickson, B.J., 2000. Analysis of Drosophila photoreceptor axon

guidance in eye-specific mosaics. Development 127, 851–60.

Orsi, A., Razi, M., Dooley, H.C., Robinson, D., Weston, a E., Collinson, L.M., Tooze, S. a, 2012. Dynamic and transient interactions of Atg9 with autophagosomes, but not membrane integration, are required for autophagy. Mol. Biol. Cell 23, 1860–73.

Paisán-Ruíz, C., Jain, S., Evans, E.W., Gilks, W.P., Simón, J., van der Brug, M., de Munain, A.L., Aparicio, S., Gil, A.M., Khan, N., Johnson, J., Martinez, J.R., Nicholl, D., Carrera, I.M., Peňa, A.S., de Silva, R., Lees, A., Martí-Massó, J.F., Pérez-Tur, J., Wood, N.W., Singleton, A.B., 2004. Cloning of the Gene Containing Mutations that Cause PARK8-Linked Parkinson's Disease. Neuron 44, 595–600.

Peter, B.J., Kent, H.M., Mills, I.G., Vallis, Y., Butler, P.J.G., Evans, P.R., McMahon, H.T., 2004. BAR domains as sensors of membrane curvature: the amphiphysin BAR structure. Science 303, 495–499.

Plowey, E.D., Cherra, S.J., Liu, Y.-J., Chu, C.T., 2008. Role of autophagy in G2019S-LRRK2-associated neurite shortening in differentiated SH-SY5Y cells. J. Neurochem. 105, 1048–56.

Pulipparacharuvil, S., Akbar, M.A., Ray, S., Sevrioukov, E. a, Haberman, A.S., Rohrer, J., Krämer, H., 2005. Drosophila Vps16A is required for trafficking to lysosomes and biogenesis of pigment granules. J. Cell Sci. 118, 3663–3673.

Pulver, S.R., Pashkovski, S.L., Hornstein, N.J., Garrity, P. a, Griffith, L.C., 2009. Temporal dynamics of neuronal activation by Channelrhodopsin-2 and TRPA1 determine behavioral output in Drosophila larvae. J. Neurophysiol. 101, 3075–88.

Puri, C., Renna, M., Bento, C.F., Moreau, K., Rubinsztein, D.C., 2013. Diverse

autophagosome membrane sources coalesce in recycling endosomes. Cell 154, 1285–99.

Quadri, M., Fang, M., Picillo, M., Olgiati, S., Breedveld, G.J., Graafland, J., Wu, B., Xu, F., Erro, R., Amboni, M., Pappatà, S., Quarantelli, M., Annesi, G., Quattrone, A., Chien, H.F., Barbosa, E.R., Oostra, B. a, Barone, P., Wang, J., Bonifati, V., 2013. Mutation in the SYNJ1 gene associated with autosomal recessive, early-onset Parkinsonism. Hum. Mutat. 34, 1208–15.

Ragusa, M.J., Stanley, R.E. and Hurley, J.H. 2012. Architecture of the Atg17 Complex as a Scaffold for Autophagosome Biogenesis. Cell 151, 1501–1512.

Ringstad, N., Gad, H., Löw, P., Di Paolo, G., Brodin, L., Shupliakov, O., De Camilli, P., 1999. Endophilin/SH3p4 Is Required for the Transition from Early to Late Stages in Clathrin-Mediated Synaptic Vesicle Endocytosis. Neuron 24, 143–154.

Rusten, T.E., Rodahl, L.M.W., Pattni, K., Englund, C., Samakovlis, C., Dove, S., Brech, A., Stenmark, H., 2006. Fab1 Phosphatidylinositol 3-Phosphate 5-Kinase Controls Trafficking but Not Silencing of Endocytosed Receptors 17, 3989–4001.

Schuske, K.R., Richmond, J.E., Matthies, D.S., Davis, W.S., Runz, S., Rube, D.A., van der Bliek, A.M., Jorgensen, E.M., 2003. Endophilin Is Required for Synaptic Vesicle Endocytosis by Localizing Synaptojanin. Neuron 40, 749–762.

Scott, R.C., Schuldiner, O., Neufeld, T.P., 2004. Role and regulation of starvation-induced autophagy in the Drosophila fat body. Dev. Cell 7, 167–78.

Soukup, S.F., Pocha, S.M., Yuan, M., Knust, E., 2013. DLin-7 is required in postsynaptic lamina neurons to prevent light-induced photoreceptor degeneration in drosophila. Curr. Biol. 23, 1349–1354.

Takahashi, Y., Meyerkord, C.L., Hori, T., Runkle, K., Fox, T.E., Kester, M., Loughran, T.P., Wang, H.-G., 2011. Bif-1 regulates Atg9 trafficking by mediating the fission of Golgi membranes during autophagy. Autophagy 7, 61–73.

Titlow, J.S., Rice, J., Majeed, Z.R., Holsopple, E., Biecker, S., Cooper, R.L., 2014. Anatomical and genotype-specific mechanosensory responses in Drosophila melanogaster larvae. Neurosci. Res. 83, 54–63.

Tong, Y., Yamaguchi, H., Giaime, E., Boyle, S., Kopan, R., Kelleher, R.J., Shen, J., 2010. Loss of leucine-rich repeat kinase 2 causes impairment of protein degradation pathways, accumulation of α-synuclein, and apoptotic cell death in aged mice. Proc. Natl. Acad. Sci. 107 , 9879–9884.

Trempe, J.-F., Chen, C.X.-Q., Grenier, K., Camacho, E.M., Kozlov, G., McPherson, P.S., Gehring, K., Fon, E. a, 2009. SH3 domains from a subset of BAR proteins define a Ubl-binding domain and implicate parkin in synaptic ubiquitination. Mol. Cell 36, 1034–47.

Urwyler, O., Izadifar, A., Dascenco, D., Petrovic, M., He, H., Ayaz, D., Kremer, A., Lippens, S., Baatsen, P., Guerin, C.J., Schmucker, D., 2015. Investigating CNS synaptogenesis at single-synapse resolution by combining reverse genetics with correlative light and electron microscopy. Development 142, 394–405.

Verstreken, P., Kjaerulff, O., Lloyd, T.E., Atkinson, R., Zhou, Y., Meinertzhagen, I. a., Bellen, H.J., 2002. Endophilin Mutations Block Clathrin-Mediated Endocytosis but Not Neurotransmitter Release. Cell 109, 101–112.

Verstreken, P., Koh, T.-W., Schulze, K.L., Zhai, R.G., Hiesinger, P.R., Zhou, Y., Mehta, S.Q., Cao, Y., Roos, J., Bellen, H.J., 2003. Synaptojanin Is Recruited by Endophilin to Promote Synaptic Vesicle Uncoating. Neuron 40, 733–748.

Vilain, S., Vanhauwaert, R., Maes, I., Schoovaerts, N., Zhou, L., Soukup, S., da Cunha, R., Lauwers, E., Fiers, M., Verstreken, P., 2014. Fast and Efficient Drosophila melanogaster Gene Knock-Ins Using MiMIC Transposons. G3 4, 2381–2387.

Williamson, W.R., Wang, D., Haberman, A.S., Hiesinger, P.R., 2010. A dual function of V0-ATPase a1 provides an endolysosomal degradation mechanism in Drosophila melanogaster photoreceptors. J. Cell Biol. 189, 885–99.

Wong, A.S.L., Lee, R.H.K., Cheung, A.Y., Yeung, P.K., Chung, S.K., Cheung, Z.H., Ip, N.Y., 2011. Cdk5-mediated phosphorylation of endophilin B1 is required for induced autophagy in models of Parkinson's disease. Nat. Cell Biol. 13, 568–79.

Young, A.R.J., Chan, E.Y.W., Hu, X.W., Köchl, R., Crawshaw, S.G., High, S., Hailey, D.W., Lippincott-Schwartz, J., Tooze, S. a, 2006. Starvation and ULK1-dependent cycling of mammalian Atg9 between the TGN and endosomes. J. Cell Sci. 119, 3888–900.

FIGURE LEGENDS

Figure 1. Autophagy is activated by metabolic and neuronal stimulation at synaptic boutons

(**A-F**) Live imaging (**A,B,D,E**) of fed (**A,D**) and 4 h-starved (**B,E**) NMJ boutons overexpressing Atg8^{mCherry} (**A-B'**) or Lamp^{GFP} (**D-E'**) under control of the *D42-Gal4* or when expressing Atg8^{mCherry} at endogenous levels (**C**); Atg8 dots (arrows). Fluorescence intensities shown using indicated scale in (**A**) and (**D**). (**C,F**) Quantification of Atg8^{mCherry} dots (arrows) (overexpression: magenta, endogenous: green) and Lamp1^{GFP} intensity; Error bars, mean ± SEM. (**C**) ANOVA Kruskal-Wallis Dunn's: ****p < 0.0001; n >11; (**F**) Mann Whitney: ****p < 0.0001, n >12 image fields per genotype.

(**G-J**) Imaging of synaptic boutons labeled with anti-mCherry or anti-GFP and expressing the TrpA1 channel under control of *D42-Gal4* (**G-G'',I-I''**) or not (*D42-Gal4*, **H,H',J,J'**) and Atg8^{mCherry} (**G-G'',H-H'**) or Lamp^{GFP} (**I-I'',J-J'**) either at 20 °C (**G,H,I,J**) or at 30 °C for 20 min (**G',I'**) or 30 min (**G'',I'',H',J'**). (**H''**) Quantification of Atg8^{mCherry} dots (arrows) and statistics with ANOVA Kruskal-Wallis Dunn's multiple comparisons ****p < 0.0001, ns p>0.05; n >11 image fields per genotype. Error bars: mean ± SEM (**J''**). Quantification of Lamp^{GFP} intensity and statistical analysis with ANOVA Tukey's multiple comparisons ****p < 0.0001, p>0.05; n >13 image fields per genotype. Individual data points and mean ± SEM is indicated.

(**K,K'**) Atg8^{mCherry} imaging following 30 min of 20 Hz electrical nerve stimulation. Dots and quantification of Atg8^{mCherry} dots (arrows) **(K'')** and statistics with Mann Whitney test ****p < 0.0001, n >10 image fields per genotype. Individual data points and mean ± SEM is indicated. Low and high intensity in magenta and green/blue (see methods). Scale bars: 10 µm (**A-B'** and **D-E'**), 5 µm (**G-K'**).

Figure 2. Correlative light and electron microscopy (CLEM) of presynaptic autophagosomes

(A-E) CLEM at boutons of starved animals expressing Atg8^{mCherry} (*D42-Gal4*). Areas around NMJs **(A)** marked by NIRB, visible in transmission and fluorescent mode **(B,C)** allows identification of this area in TEM. **(D)** NMJ boutons with Atg8^{mCherry} dots (arrows) and **(E)** correlation of fluorescent and electron micrograph of Atg8^{mCherry} positive boutons, enlarged in **(F)**. Scale bars: 1 mm **(A)**, 20 µm **(B,C)** and 5 µm **(E)**.

(F) Lowering fluorescence intensities allows correlation of Atg8^{mCherry} positive dots (in **D**) and ultrastructural features (arrows; box 1 and 2; EM-z-plane indicated in relation to images in (G)).

(G) Serial section EM of bouton 1, each z-step thickness is 100 nm. Atg8^{mCherry} positive features (arrows) are only detected in z=5 and z=6.

(H,I) Boutons '1' and '2' with Atg8^{mCherry} positive structures (arrows); z=3 **(F,I)** and z=6 **(H)** (cf. **(G)**).

(J,K) Examples of Atg8^{mCherry} CLEM at NMJs. **(J)** Atg8^{mCherry} and mito-GFP (to label mitochondria) expressed (*D42-Gal4*) and **(K)** Atg8^{mCherry} expressed from a genomic transgene. Atg8^{mCherry} positive ultrastructural features indicated by arrows (3, 4). **(H-K)** Scale bars; 500 nm.

(L) Examples of Atg8^{mCherry} positive structures identified by CLEM. Numbers 1-4 correspond to the indicated boutons.

Figure 3. Phosphomimic EndoA creates membrane zones that recruit Atg3

(A-E'') Live imaging of EndoA-dependent Atg3 recruitment to the GUVs. GUV membrane marked by DIO (green). GUVs were incubated with Atg3::mCherry (magenta) **(A-A'')** and EndoA^{S75D} **(B-C'')** or EndoA^{S75A} **(D-E'')**. EndoA^{S75D} causes more Atg3 recruitment to the membrane.

(F) Quantification of Atg3::mCherry on GUV membrane: GUVs were randomly chosen and not preselected. Statistical analysis: ANOVA Tukey's multiple comparisons *p <

0.05, ****p < 0.0001, n >10 individual data points from 2 independent experiments. Mean ± SEM. Scale bar 5 µm.

Figure 4. EndoA is necessary for macroautophagy at the synapse

(**A-A''**) Synaptic boutons at starved NMJs expressing Atg9^{GFP} (*D42-Gal4*) labeled with anti-EndoA and anti-GFP.

(**B**) Western blot of an anti-GFP IP from control fly heads (*Da-Gal4>LRRK2^{G2019S}*) and Atg9^{GFP} expressing fly heads (*Da-Gal4>Atg9^{GFP}, LRRK2^{G2019S}*) probed with anti-GFP (to assess IP specificity) and anti-EndoA (LRRK2^{G2019S} induces autophagy, see below). n=2 independent experiments.

(**C**) Schematic of EndoA with tetracystein (4C) tag and inactivation by FlAsH-mediated Fluorescein Assisted Light Inactivation (FlAsH-FALI).

(**D**) Quantification of FM 1-43 labeling intensity following EndoA inactivation by FlAsH-FALI. Animals express EndoA^{4C} at endogenous levels (*endoA^{4C}; endoA$^{+/-}$*) and were incubated in FlAsH ('+FlAsH'). EndoA was then inactivated with light or not ('+/- light'). Boutons were finally labeled using 1 min 90 mM KCl in HL3 with 1 mM $CaCl_2$ ('+ stim'). Data were analyzed using Mann Whitney test ****p < 0.0001, n >25 image fields per genotype. Individual data points and the mean ± SEM is indicated. EndoA^{4C} acts dominantly.

(E) Quantification and images (live) (**E'-E'''**) of Atg8^{mCherry} dots at boutons of controls (*w*) or *endoA^{4C}; endoA$^{+/-}$* animals that express Atg8^{mCherry} (*D42-Gal4*) incubated with FlAsH ('+FlAsH') with or without shining light on the NMJ ('+/- light') and before or after 30 min of 20 Hz electrical stimulation ('+/- stim'). Data analyzed using ANOVA Kruskal-Wallis Dunn's multiple comparisons *p<0.05, **p<0.01, ***p= <0.001, ****p < 0.0001, n >11 image fields per genotype. Individual data points and the mean ± SEM is indicated.

(**F-H**) Imaging of anti-mCherry labeled *shi^{ts1}*mutant boutons expressing Atg8^{mCherry} (*D42-Gal4*) and of control animals (Atg8^{mCherry} (*D42-Gal4*)) raised at 37 °C (restrictive temperature) for 1 h during starvation (**F-G'**). Quantification of Atg8^{mCherry} dots (arrows) (**H**)

and statistical analysis with ANOVA Kruskal-Wallis Dunn's multiple comparisions ****p < 0.0001, n >17 image fields per genotype. Individual data points and the mean ± SEM is indicated. Scale bar 5 µm.

Figure 5. EndoA S75 phosphorylation acts as a switch for autophagy

(**A-D**) Live imaging (**A-C'**) of fed (**A,B,C**) and 4 h-starved (**A',B',C'**) NMJ boutons of *endoA*$^{-/-}$ null mutants expressing *endoA*^{S75A} (**A,A'**), *endoA*^{S75D} (**B,B'**) or *endoA*^{WT} (**C,C'**) at endogenous levels and Atg8^{mCherry} with *D42-Gal4*. Quantification of Atg8^{mCherry} dots (arrows) (**D**) and statistical analysis with ANOVA Kruskal-Wallis Dunn's multiple comparisons test **p <0.01, ***p<0.001 ****<, p < 0.0001, n >11 image fields per genotype. Individual data points and the mean ± SEM is indicated.

(**E-K**) Synaptic boutons labeled with anti-mCherry and anti-HA of *w* control animals expressing Atg8^{mCherry} (magenta, **E'',F'',G'',H'',I'',J''**) and Atg3^{HA} (*D42-Gal4*) (green, **E',F',G',H',I',J'**) or *endoA* null mutants expressing *endoA*^{S75A} (**G-G'',H-H''**) or *endoA*^{S75D} (**I-I'',J-J''**) at endogenous levels. **(K)** Quantification of Pearson coefficient of Atg3^{HA} colocalization on Atg8^{mCherry} puncta in the mask of Atg8^{mCherry} puncta. Statistical analysis with ANOVA Tukey's multiple comparisons, **p <0.01, ***p<0.001 ****<, p < 0.0001; n >18 image fields per genotype. Data points and the mean ± SEM is indicated. Scale bar 5 µm.

Figure 6. LRRK2 kinase activity is required for autophagy at the synapse

(**A-A''**) NMJ boutons of *LRRK*^{HA} knock-in flies labeled with anti-HA antibodies (magenta) and anti-EndoA (green). Inserts show magnification.

(**B-F**) Live imaging of fed (**B,C,D,E**) and 4 h-starved (**B',C',D',E'**) NMJ boutons of *w* control animals (**B-B'**), *lrrk* mutants (**C-C'**) and *lrrk* mutants with a genomic *lrrk* rescue construct **(D-D')** and *lrrk* mutants expressing human LRRK2 and Atg8^{mCherry} (*D42-Gal4*) (**E-E')**. (**F**) Quantification of Atg8^{mCherry} dots per bouton area (arrows) and statistical analysis with ANOVA Kruskal-Wallis Dunn's multiple comparisons ****p < 0.0001, n >12 image fields per genotype. Individual data points and the mean ± SEM is indicated.

(**G-I**) Control (*TrpA1,* **G,G'**) and *lrrk* mutant (*TrpA1, lrrk*$^{-/-}$, **H,H'**) synaptic boutons labeled with anti-mCherry and expressing the TrpA1 channel and Atg8^{mCherry} (*D42-Gal4*) either kept at 20 °C (**G,H**) or raised to 30 °C for 30 min (**G',H'**). Quantification of the Atg8^{mCherry} dots (arrows) (**I**). Statistical analysis with ANOVA Kruskal-Wallis Dunn's multiple comparisons test ***p < 0.001, n >10 image fields per genotype. Individual data points and the mean ± SEM is indicated.

(**J-L**) Live NMJ boutons of wild type animals that express kinase active LRRK2^{G2019S} (**J-J'**) or the kinase dead LRRK2^{D2017A} (**K-K'**) and Atg8^{mCherry} (*D42-Gal4*) in fed (**J,K**) and 4 h-starved (**J',K'**) conditions. Quantification of Atg8^{mCherry} dots (arrows) (**L**) and statistical analysis with ANOVA Tukey's multiple comparison *p<0.05, **p<0.01, ***p <0.001, n >11 image fields per genotype. Individual data points and the mean ± SEM is indicated. (**B-E',G-H',J-K'**). Scale bars: 10 µm (**A-A''**) or 5 µm (**B-E',G-H',J-K'**).

Figure 7. EndoA acts downstream of LRRK in autophagy

(**A-C'**) Live imaging of fed (**A-C**) and 4 h-starved (**A'-C'**) boutons of *lrrk*$^{-/-}$ expressing at endogenous levels *endoA*^{S75D} (**A,A'**) or *endoA*^{S75A} (**B,B'**) and Atg8^{mCherry} (*D42-Gal4*) and *endoA*$^{-/-}$ null mutants expressing *endoA*^{S75A} at endogenous levels and overexpressing LRRK2^{G2019S} (**C,C'**) and Atg8^{mCherry} (*D42-Gal4*).

(**D**) Quantification of Atg8^{mCherry} dots (arrows; **A,A'**) and statistical analysis with ANOVA Kruskal-Wallis Dunn's multiple comparisons ***p<0.001, ****p <0.0001, n >11 image fields per genotype. Individual data points and the mean ± SEM is indicated. Scale bar 5 µm.

Figure 8. EndoA phosphorylation balance is critical for neuronal survival

(**A-B'**) ERG traces of control (*w*) and flies with *endoA*$^{-/-}$ mutant eyes (raw data grey, average black) in response to a 1 s light pulse of flies kept for 7 days in constant dark (**A,B**) or for 3 days in constant light (**A',B'**). Green bar: amplitude of the depolarization and

deterioration of this response (arrow). Asterisk: flies with *endoA*$^{-/-}$ null mutant eyes lack on and off transients.

(**C, D**) Histological sections of retinas after 7 days of continuous light exposure, genotypes in (**A-B'**). Arrows: loss of rhabdomeres. Scale bars (for **C,D,M-O**): 5 μm.

(**E, F**) EM micrographs of lamina photoreceptor terminals after 7 days of continuous light exposure, genotypes in (**A-B'**). Violet: photoreceptor terminals, Green: postsynaptic neurons, Yellow: terminals showing degeneration. Constant dark data in the supplemental section. Scale bars (for **E,F,P-R**): 2 μm.

(**G**) Quantification of ERG depolarization amplitude in light or dark reared flies (see **A-B'**). Samples were compared using ANOVA-Kruskal Wallis Dunn's multiple comparisons tests ** p<0.01;****p <0.0001: Bars: mean +SEM. For **G** and **S**: genotypes were compared using ANOVA Kruskal Wallis followed by Dunn's multiple comparisons tests ***p<0.001 **p<0.01 *p<0.05; n >12. Bars: mean ± SEM.

(**H**) Quantification of the number of rhabdomers per ommatidia in light or dark reared flies (see **C-D**). For **H** and **T**: samples were compared using ANOVA-Kruskal Wallis post hoc Dunn's multiple comparisons tests ****p <0.0001, n >64. Bars: mean ± SEM.

(**I**) Quantification of the number of photoreceptor terminals per lamina cartridge in light or dark reared flies (see **E-F**). For **I** and **U**: samples were compared using ANOVA-Kruskal Wallis post hoc Dunn's multiple comparisons tests ****p <0.0001, n >60. Bars: mean ± SEM. (**C,D,M-O**) Scale bars 5 μm. (**E,F,P-R**) Scale bars 2 μm.

(**J-L'**) ERG traces of *cn bw* control flies (**J,J'**), *endoA* mutant flies expressing *endoA*^{S75A} (**K,K'**) or *endoA*^{S75D} (**L,L'**) at endogenous levels, as in (**A-B'**).

(**M-O)** Histological sections of retinas after 7 days of continuous light exposure, genotypes in (**J-L'**), as in (**C, D**).

(**P-R**) EM micrographs of lamina photoreceptor terminals after 7 days of continuous light exposure, genotypes in (**J-L'**), as in (**E, F**).

(**S-U**) Data shown in (**J-R**) for light and dark reared flies (also see supplemental data section).

Figure 1

Click here to download Figure Fig1_neuron_rev_x.tif

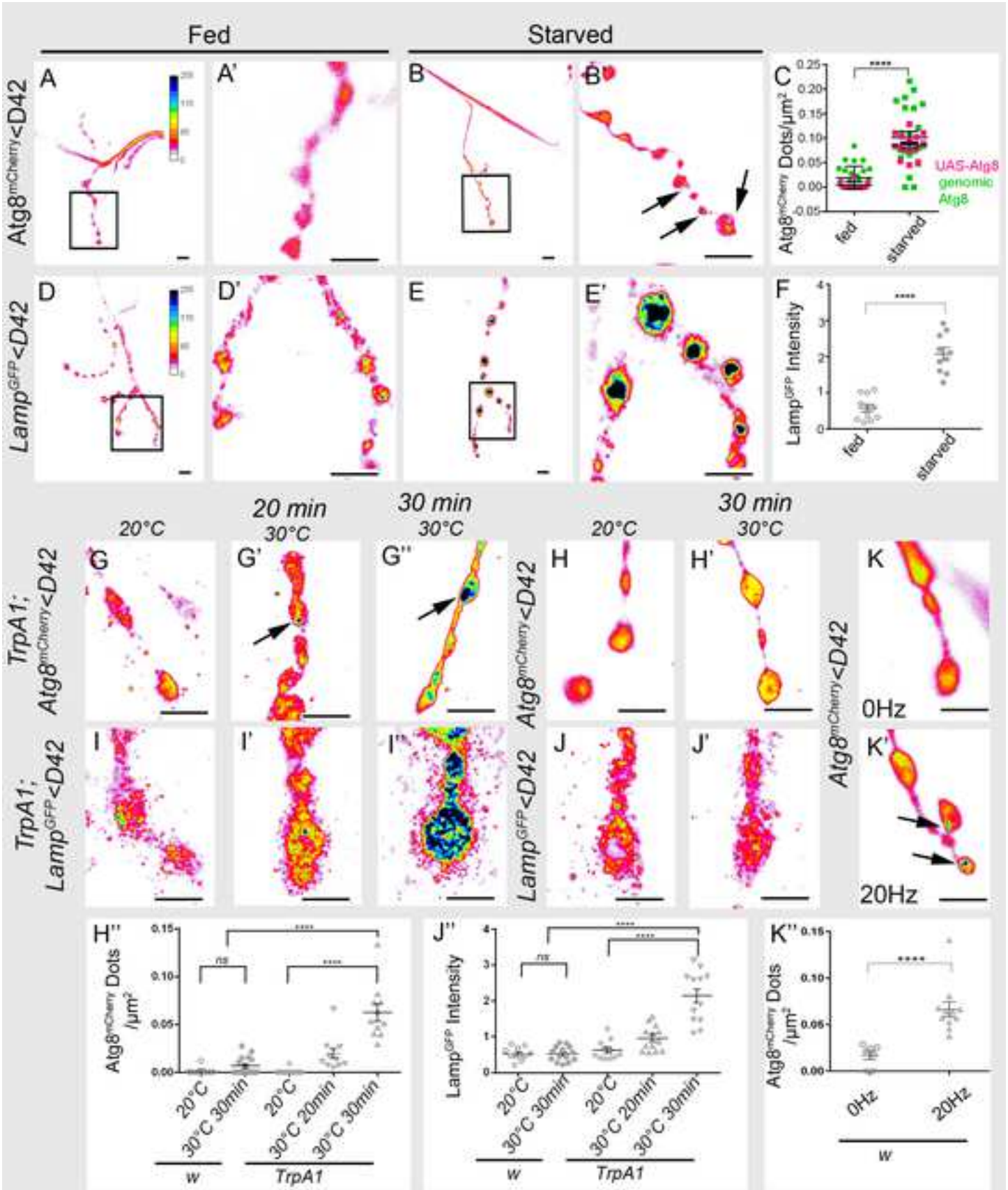

Figure 2

Click here to download Figure Fig2_neuron_rev_2.tif

Fig. 2

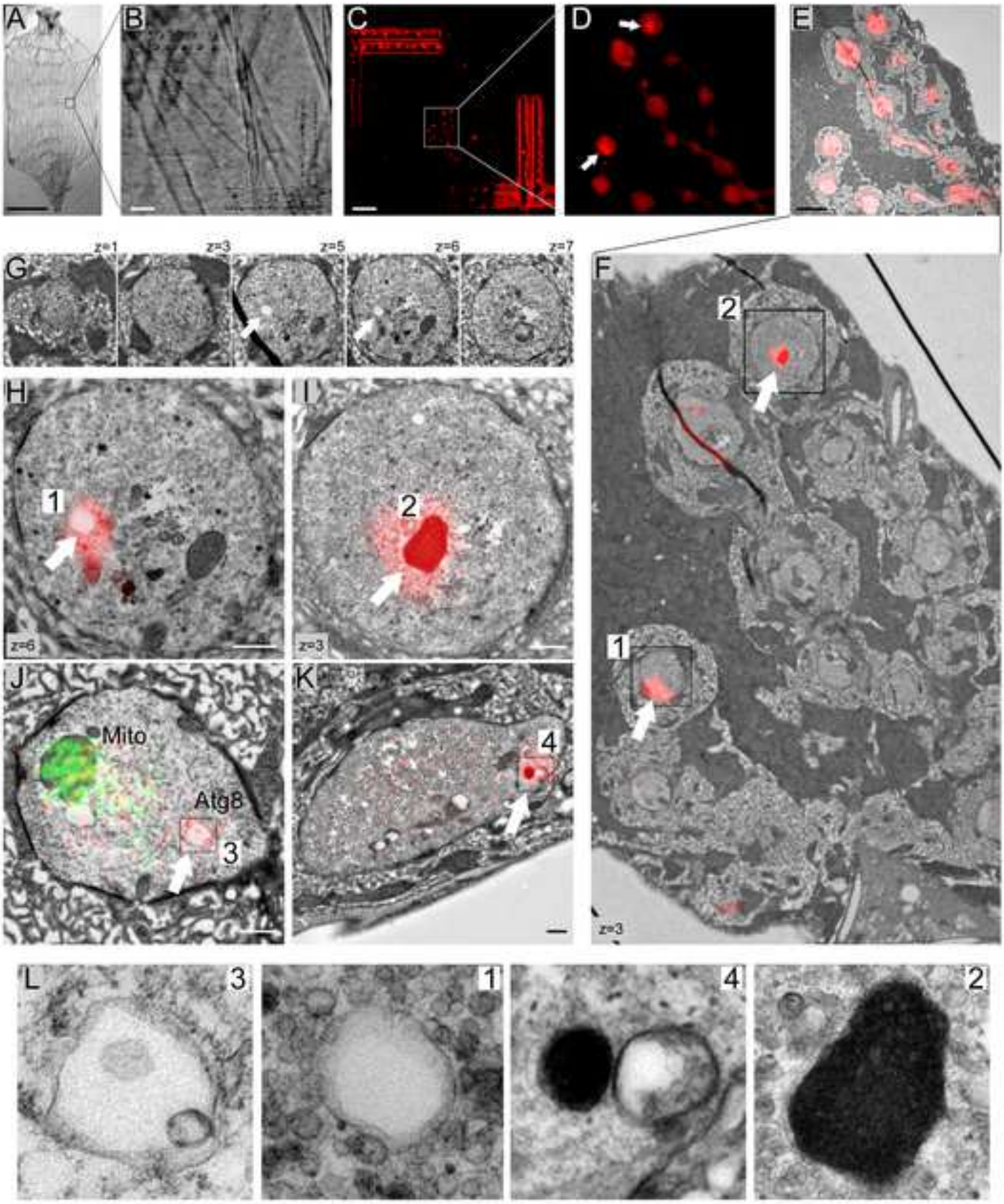

Figure 3

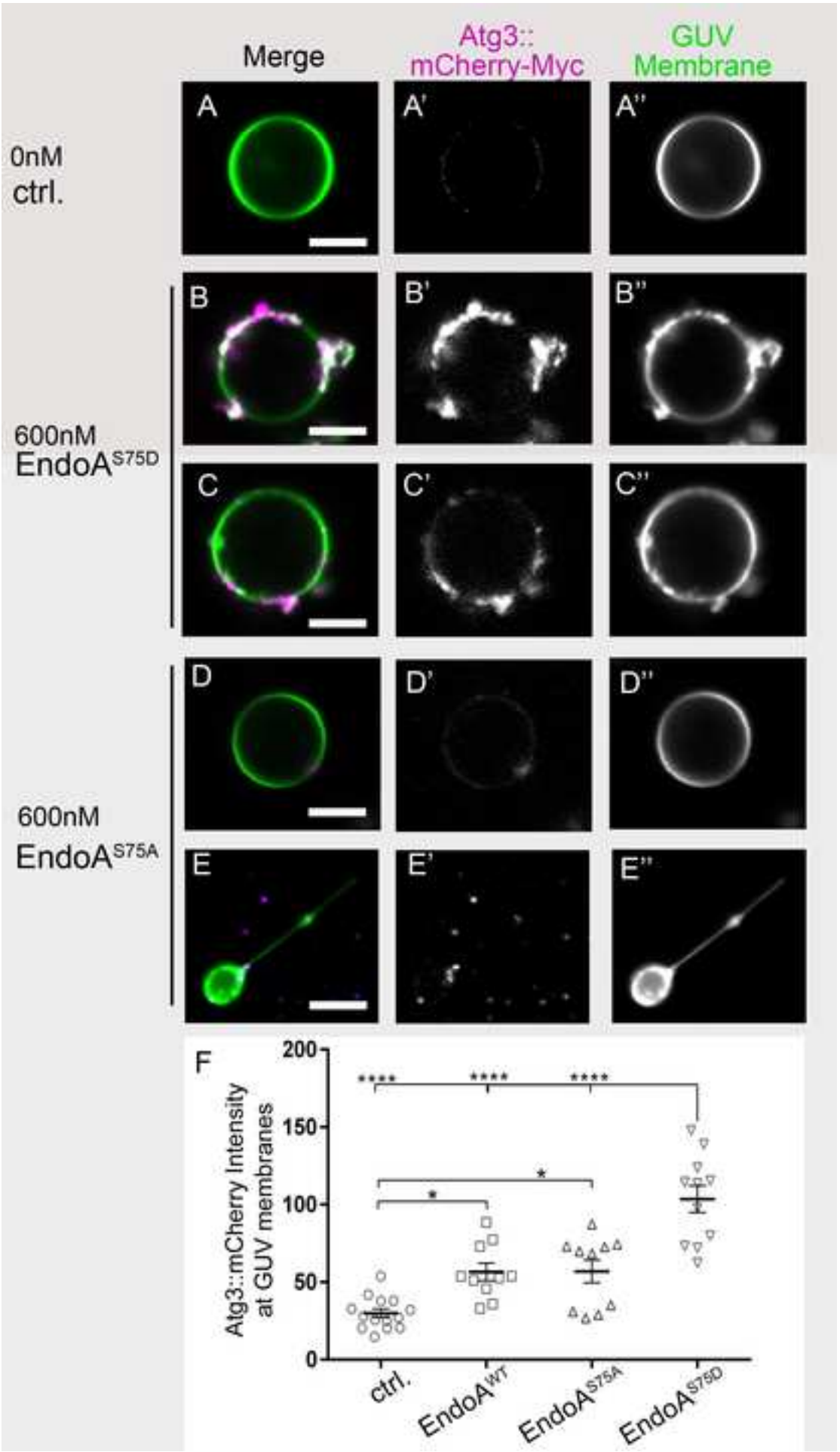

Figure 4

Click here to download Figure Fig4_neuron_rev.tif

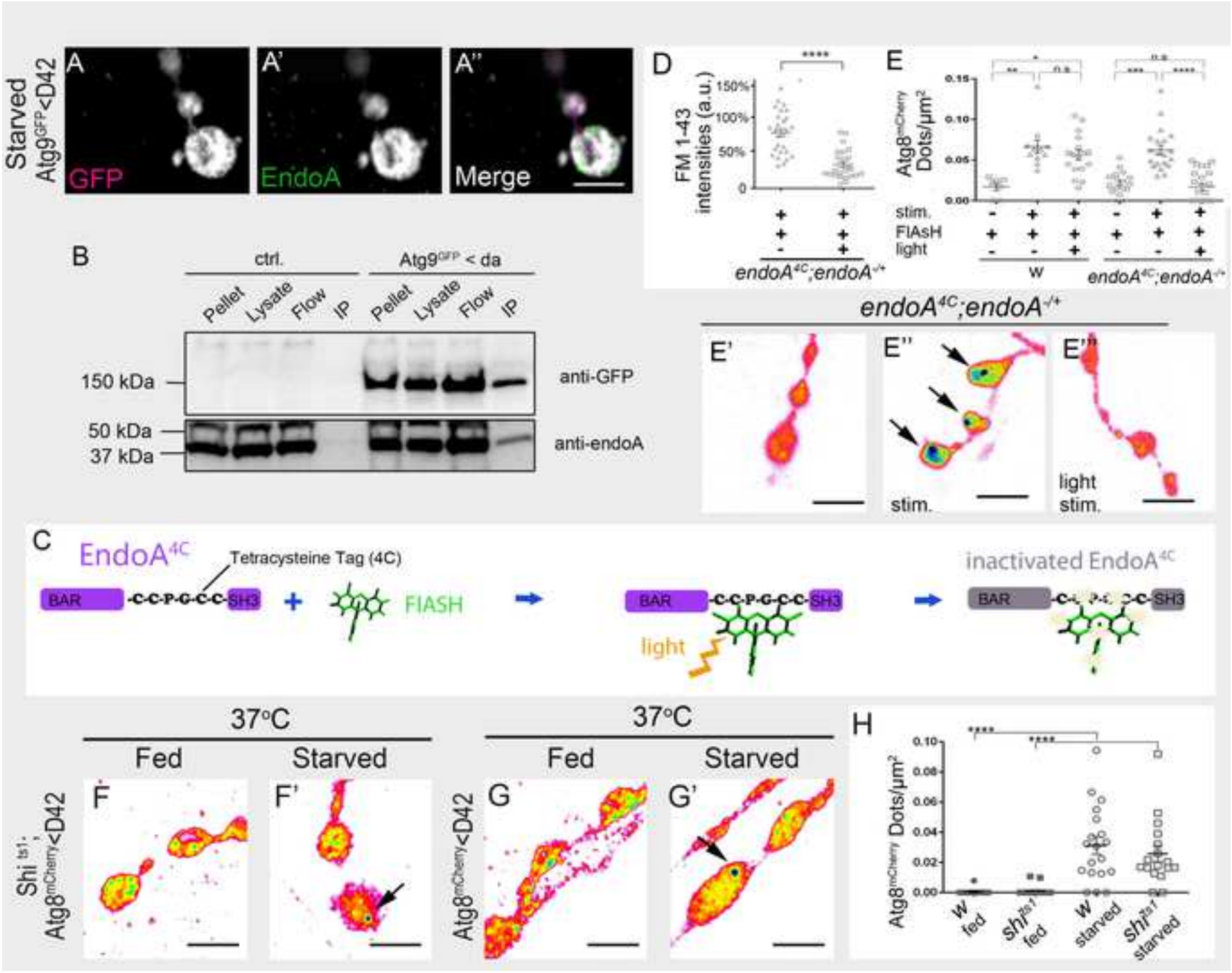

Figure 5

Click here to download Figure Fig5_neuron_rev.tif

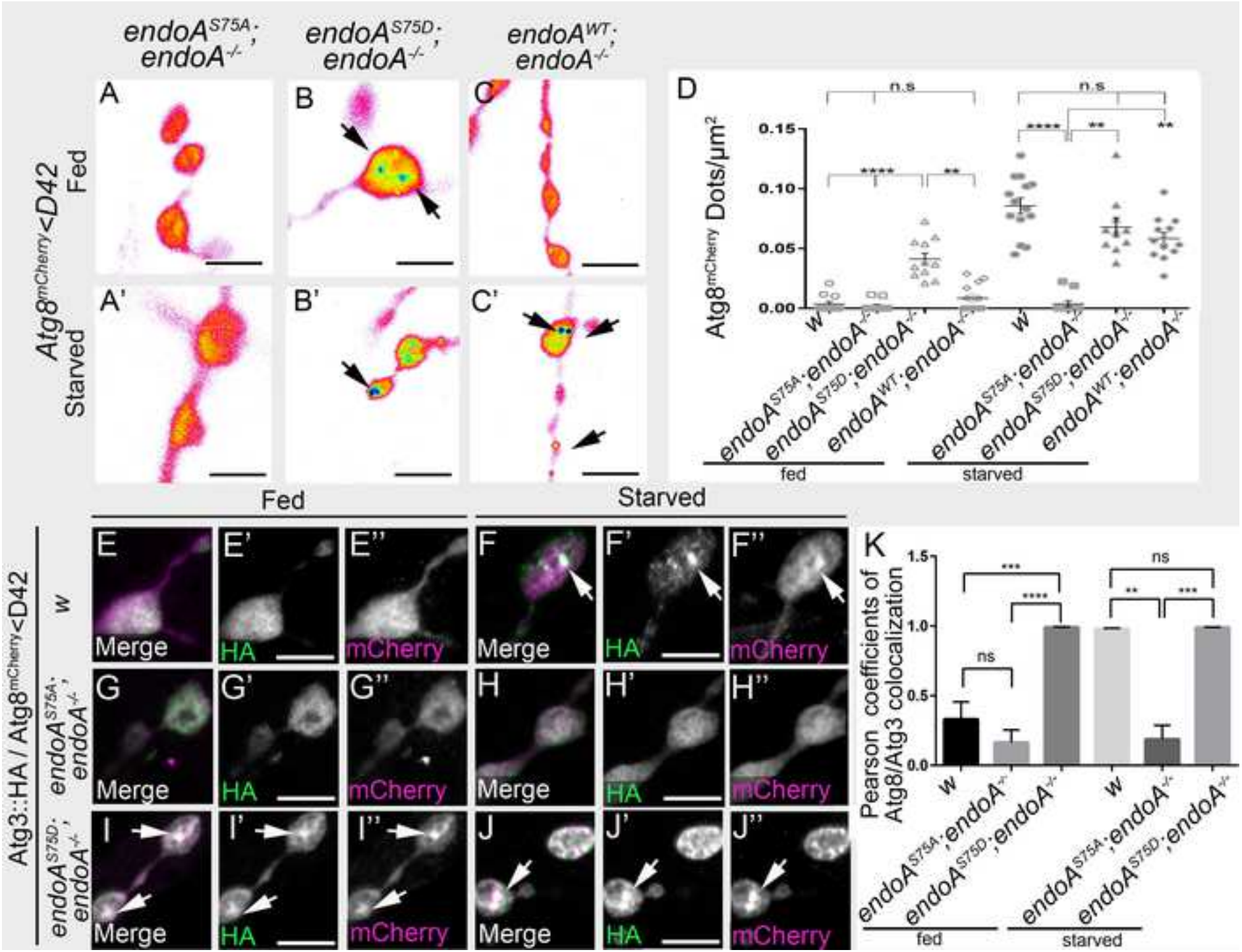

Figure 6

Click here to download Figure Fig6_neuron_rev.tif

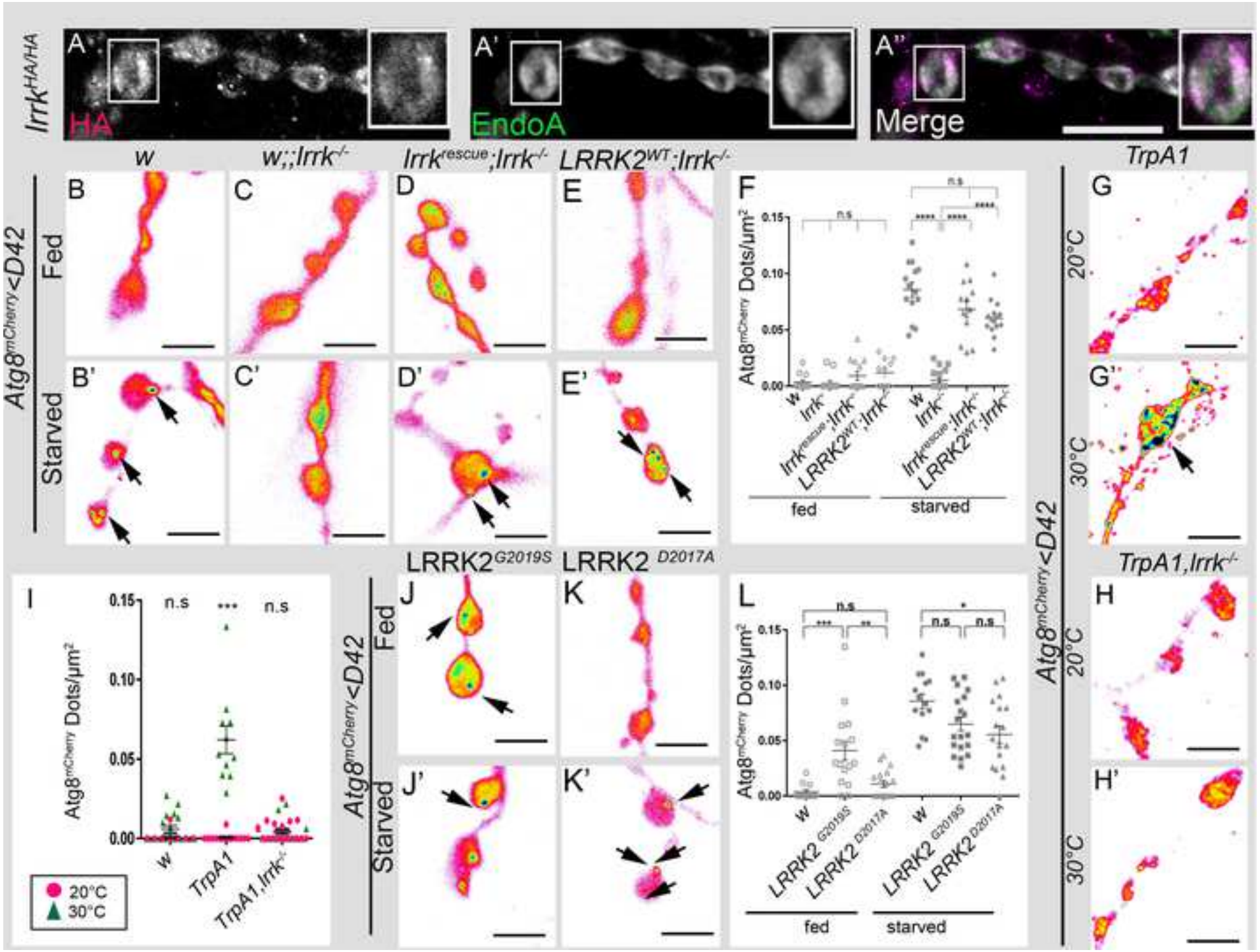

Figure 7

Click here to download Figure Fig7_neuron_rev.tif

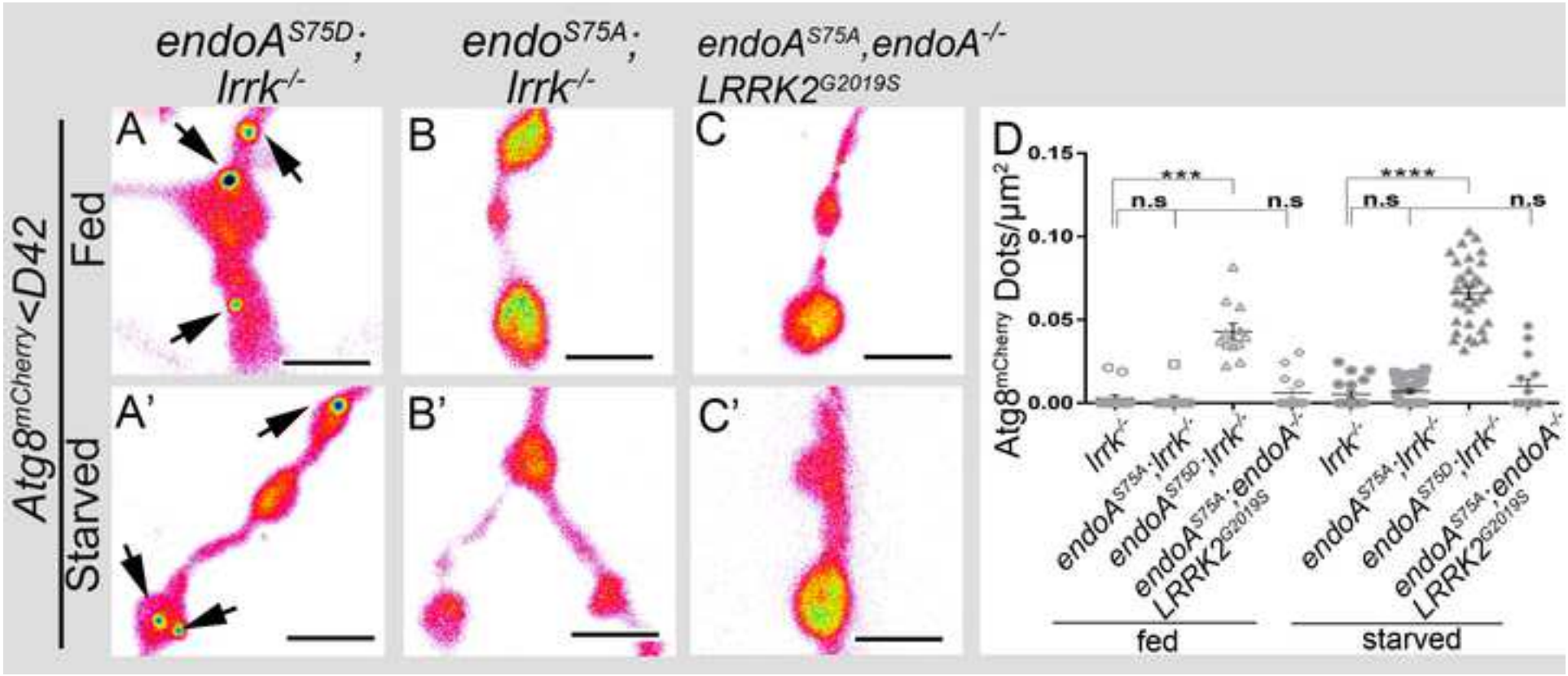

Figure 8

Click here to download Figure Fig8_neuron_rev.tif

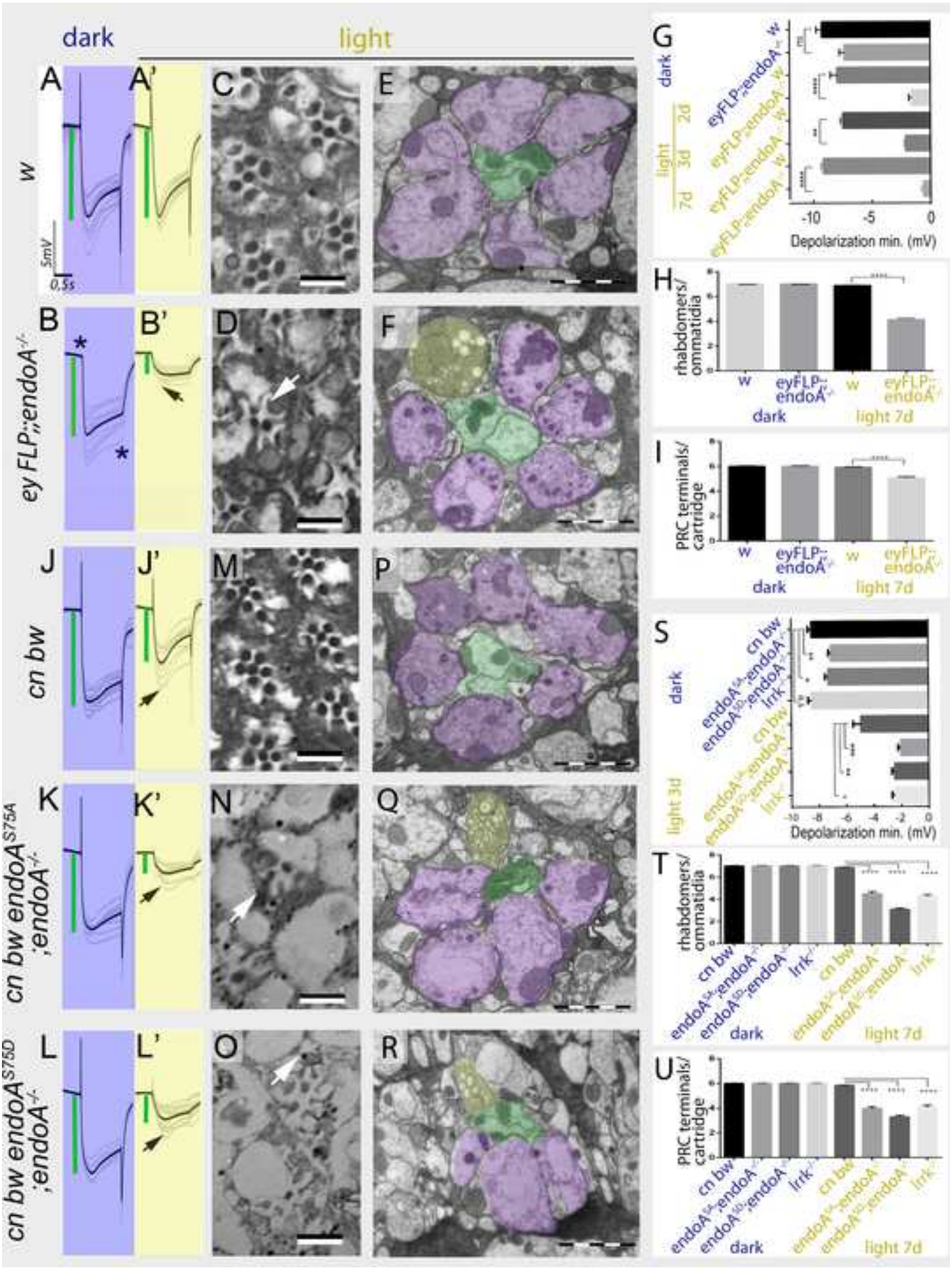

SUPPLEMENTAL INFORMATION

SUPPLEMENTAL FIGURES

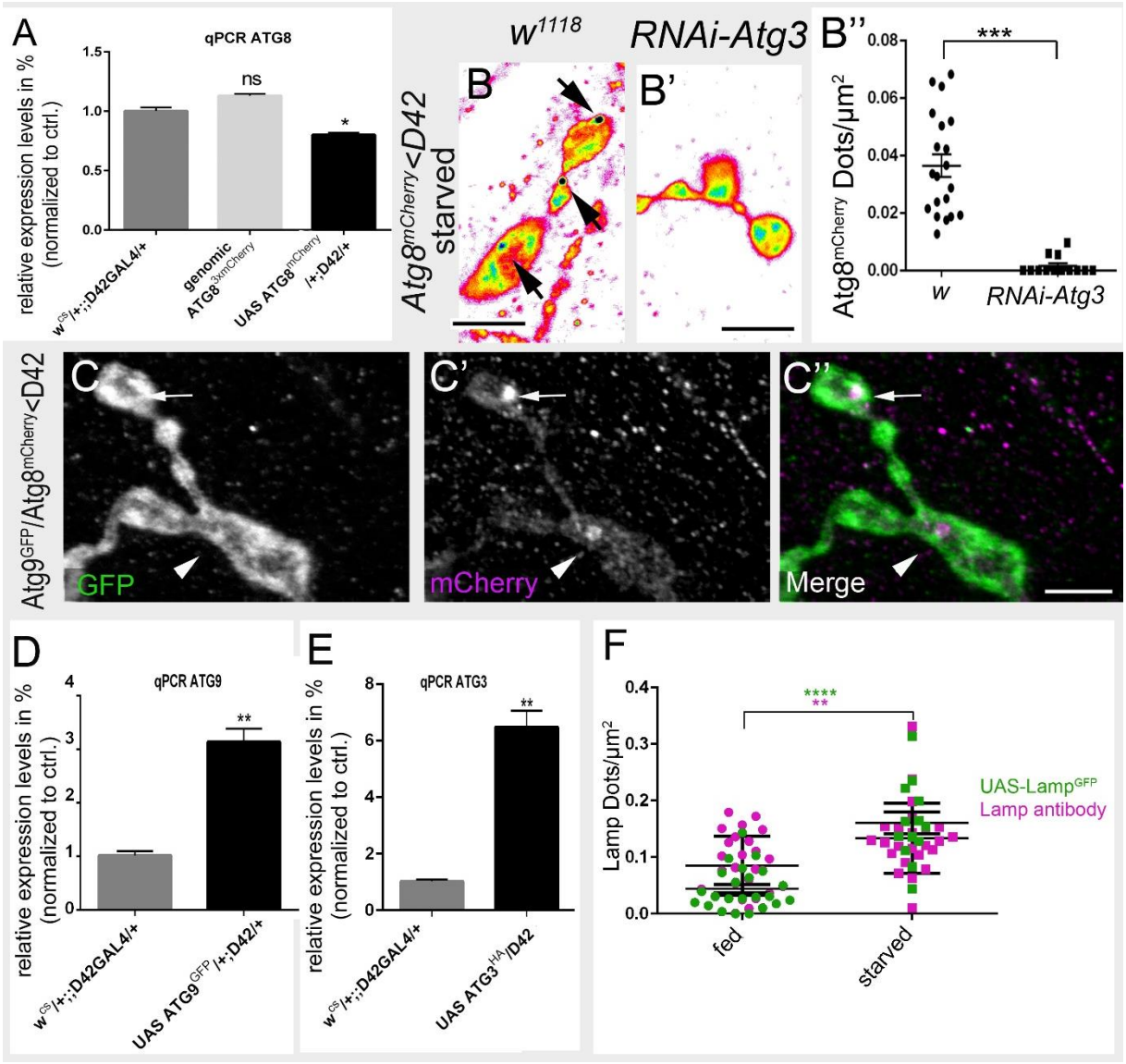

Figure S1. Autophagic markers at *Drosophila* NMJ boutons, related to Figure 1

(A) Quantitative RT PCR to assess Atg8 expression levels in controls (w^{cs}/+; *D42 Gal4*/+), animals with a genomic Atg8^{3xmCherry} (genomic *Atg8^{3xmCherry}*) and flies over expressing Atg8^{mCherry} using *D42-Gal4* in motor neurons. Data sets were analyzed using 1-way ANOVA-Kruskal-Wallis test followed by a post hoc Dunn's test, p=0.0338, n=6 repetitions; error bars= Mean+SEM.

(B,B'') Images of anti-mCherry labeling (to reveal Atg8 dots) of neuromuscular junction boutons of w control animals **(B)** and of animals expressing RNAi against Atg3 (*D42-Gal4*) **(B').** Atg8^{mCherry} was expressed under the

control of the *D42-Gal4* driver. (**B''**) Quantification of the number of $Atg8^{mCherry}$ dots using Mann Whitney test, $p < 0.001$, $n > 13$ image fields per genotype ; error bars= Mean+SEM.

(C-C'') Images of starved neuromuscular junction (NMJ) boutons expressing $Atg9^{GFP}$ (green) **(C)** and $Atg8^{mCherry}$ (magenta) (**C''**) (*D42-Gal4*). Atg8 accumulation marked by an arrow (co-localization) or arrowhead (no/less co-localization). Scale bars: 5 µm.

(D) Quantitative RT-PCR to assess Atg9 expression levels in controls (w^{cs}/+; D42 Gal4/+) and in flies over expressing $Atg9^{GFP}$ driven by *D42-Gal4*.

(E) Quantitative RT-PCR to assess Atg3 expression levels in controls (w^{cs}/+; D42 Gal4/+) and in flies over expressing $Atg3^{3xHA}$ driven by *D42-Gal4*. Both data sets in **D** and **E** were analyzed with Mann-Whitney test $p<0.01$, n=6 repetitions; error bars= Mean+SEM.

(F) Quantification of the number of Lamp dots at synaptic boutons expressing UAS-$Lamp1^{GFP}$ in motor neurons (*D42-Gal4*) and of Lamp dots in boutons labeled with anti-Lamp. Data were analyzed with Mann-Whitney test (for the anti-dLAMP dots: $p <0.01$ and for UAS $LAMP^{GFP}$ $p < 0,0001$, $n>15$ image fields per genotype; error bars= Mean+SEM).

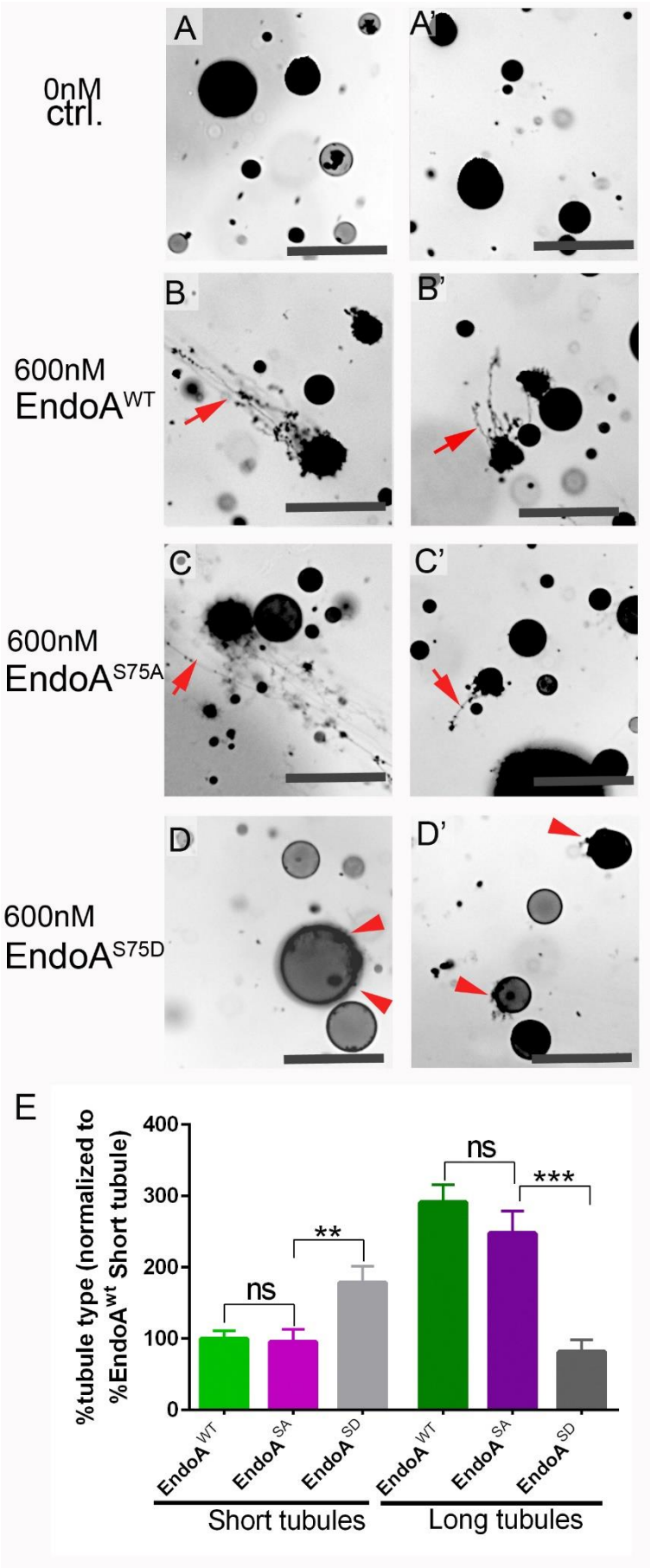
0nM
ctrl.
A
A'
600nM
EndoA^WT
B
B'
600nM
EndoA^S75A
C
C'
600nM
EndoA^S75D
D
D'
E
%tubule type (normalized to
%EndoA^wt Short tubule)
400
300
200
100
0
ns
**
ns
***
EndoA WT
EndoA SA
EndoA SD
EndoA WT
EndoA SA
EndoA SD
Short tubules
Long tubules

Figure S2. S75 phosphorylation changes membrane deformation activity of EndoA on PI(3)P containing GUVs, related to Figure 3

(**A-C**) Images of PI(3)P containing GUVs that were generated using the protocol identical to the GUVs used in Figure 3 (Atg3 recruitment assay). The membrane of the GUVs was marked by incorporation of the lipid dye DIO. GUVs were incubated with Buffer (ctrl.) **(A-A')**, 600 nM EndoA^{WT} **(B-B')**, 600 nM EndoA^{S75A} **(C-C')** or 600 nM EndoA^{S75D} **(D-D')**. Note that EndoA^{S75D} forms short tubules, narrow membrane bends or vesicular structures on GUVs (red arrowheads), while EndoA^{WT} and EndoA^{S75A} (arrows) form long tubules on GUVs. Scale bar 50 µm. **(E)** Quantification of tubule types normalized to EndoA^{WT} short tubules. Tubules were categorized as short tubules or membrane bends (arrowheads) and long tubules (arrows). Data were analyzed using 1way ANOVA followed by a post hoc Tukey test, **p <0,01, *** p<0,001, n=12 image fields per condition; error bars = mean ± SEM.

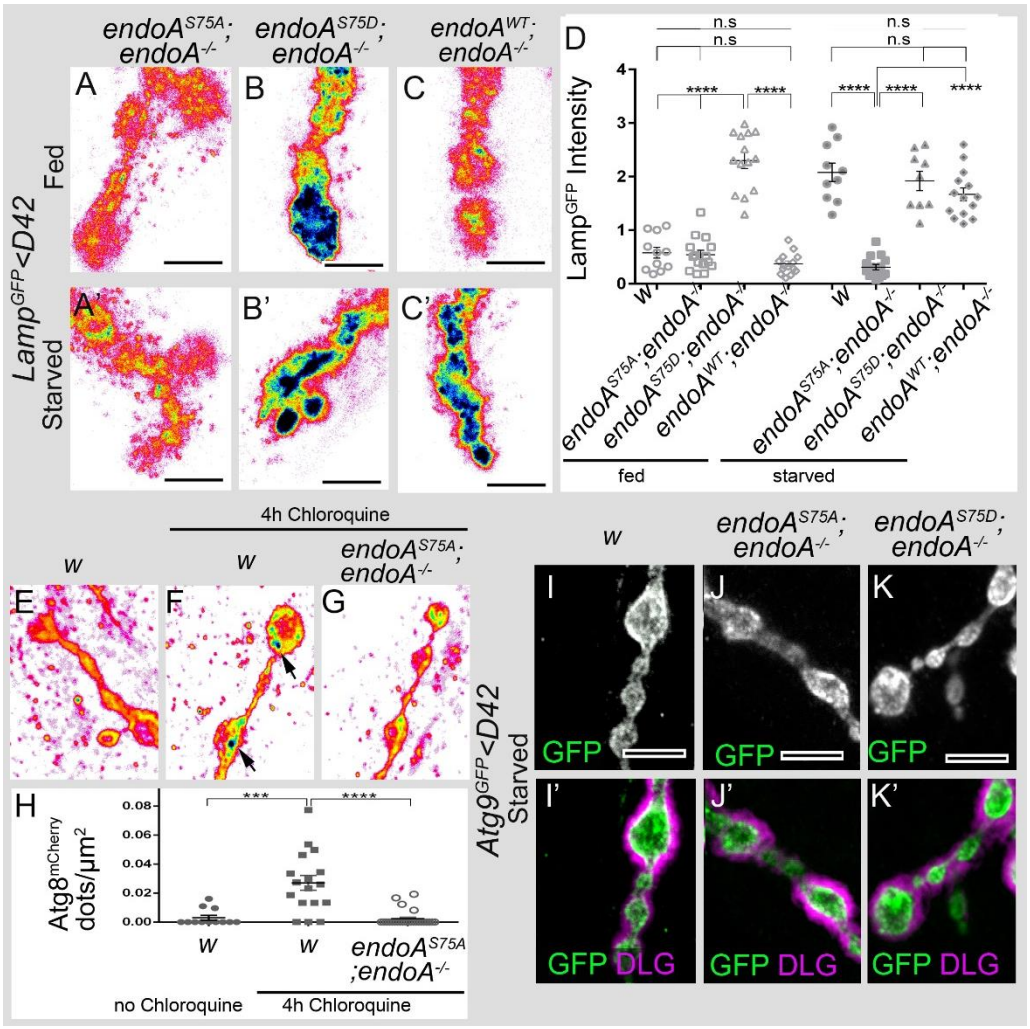

Figure S3. EndoA function on preautophagosomes is essential for synaptic autophagy, related to Figure 5

(A-C') Live imaging of fed **(A,B,C)** and 4h-starved **(A',B',C')** NMJ boutons of *endoA*$^{-/-}$ null mutants expressing *endoA*^{S75A} **(A-A')**, *endoA*^{S75D} **(B-B')** or *endoA*^{wt} **(C-C')** at endogenous levels and expressing Lamp^{GFP} under the control of the *D42-Gal4* driver. Quantification of Lamp^{GFP} boutonic intensity **(D)** of the indicated genotypes and statistical analysis using 1 way ANOVA followed by Post Hoc Tukey's multiple comparisons test ****p < 0.0001, n >10 image fields per genotype. Note that phosphodead EndoA blocks synaptic autophagy and phosphomimetic EndoA constitutively induces it. Individual data points are shown and the mean ± SEM is indicated. **(E-G)** Autophagic flux assay at the NMJ under fed conditions of control animals **(E),** control animals 4h fed with Chloroquine **(F)** and *endoA*$^{-/-}$ null mutants expressing *endoA*^{S75A} 4h fed with Chloroquine **(G)**. Quantification of Atg8^{mCherry} positive puncta **(H)** of the indicated genotypes and statistical analysis using 1-way ANOVA-Kruskal Wallis followed by a post hoc Dunn's multiple comparisons test ***p< 0.001,****p<0.0001; n >12 image fields per genotype. Individual data points are shown and the mean ± SEM is indicated. Fluorescence intensities are shown using the scale indicated in Figure 1. **(I-K')** NMJ boutons of control animals **(I-I'),** *endoA*$^{-/-}$ null mutants expressing *endoA*^{S75A} **(J-J')** or *endoA*^{S75D} **(K-K')** at endogenous levels and expressing Atg9^{GFP} under the control of *D42-Gal4* driver. After starvation third instar larvae were dissected and labeled with anti-GFP (green, **I,J,K**) and anti-DLG (magenta, **I',J',K'**). Scale bar 5 µm.

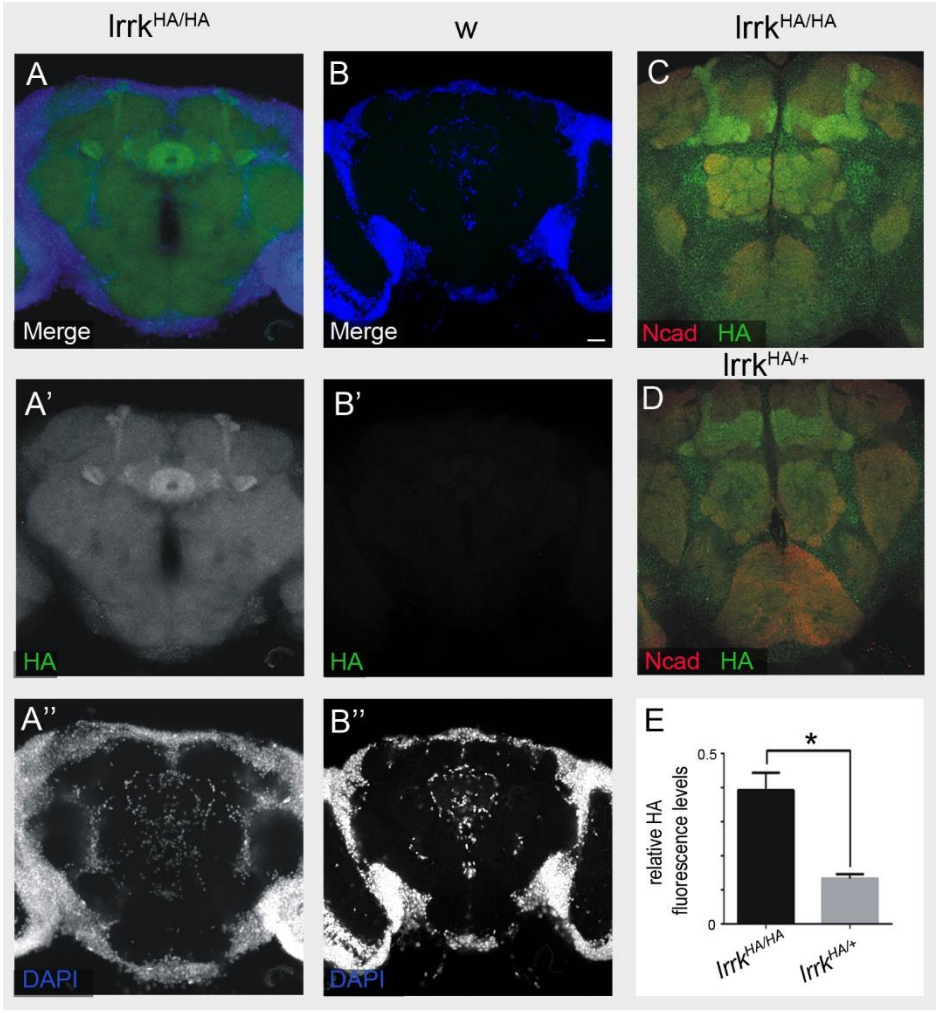

Figure S4. Expression and specificity of LRRK-HA labeling and rescue experiments, related to Figure 6

(**A-B**) Central fly brains of *lrrk*$^{HA/HA}$ animals (**A-A''**) and *w* controls (**B-B''**) labeled with anti-HA (**A', B'**) and DAPI (**A'', B''**) indicates specificity of LRRK^{HA} labeling.

(**C-E**) Central fly brains of *lrrk*$^{HA/HA}$ (**C**) and *lrrk*$^{HA/+}$ (**D**) labeled with anti-HA and anti-NCad to label the neuropile. (**E**) Quantification of labeling intensity by Mann Whitney test *p<0.05, n =6 brains per genotype, the mean ± SEM is indicated. Note that heterozygous *lrrk*$^{HA/+}$ animals express about half as much LRRK^{HA} compared to homozygous animals (**E**). Scale bar 20 µm.

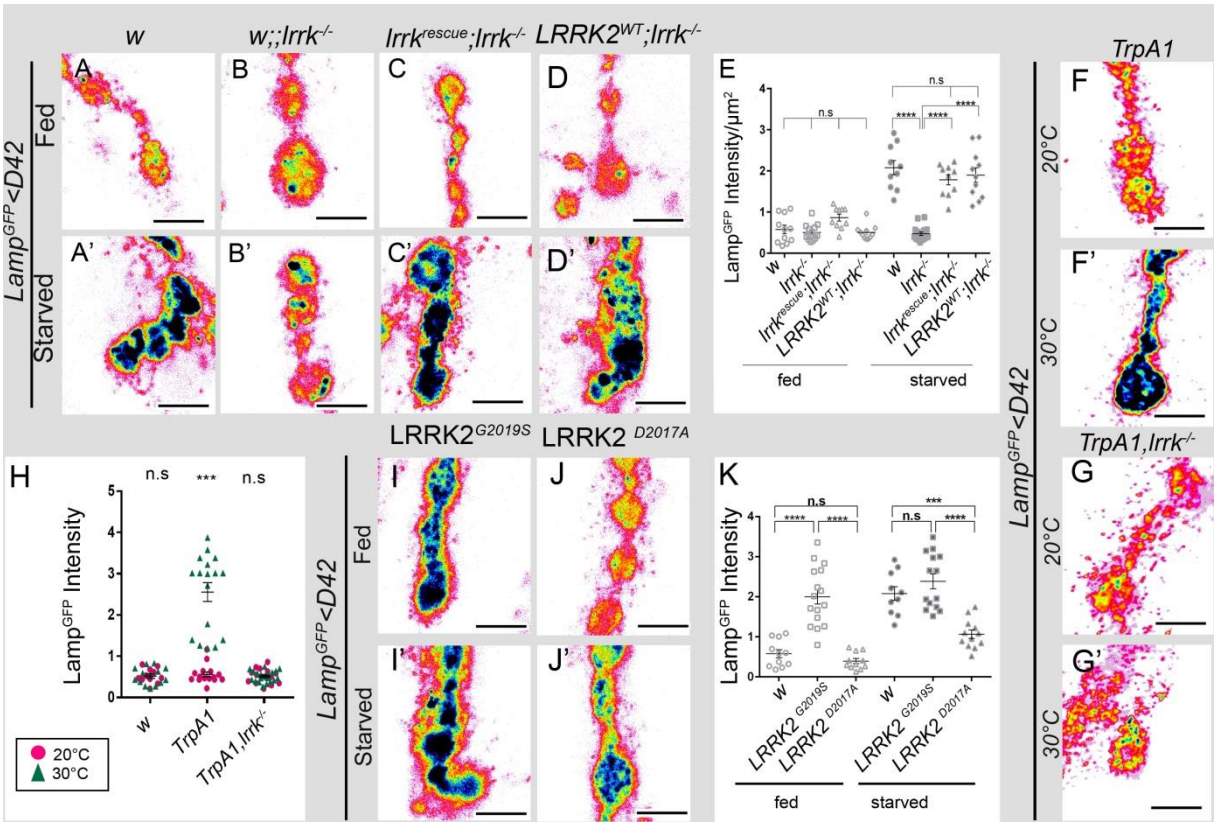

Figure S5. LRRK2 kinase activity is required for autophagy at synapses, related to Figure 6

(A-E) Live imaging of fed **(A,B,C,D)** and 4 h-starved **(A',B',C',D')** NMJ boutons of *w* control animals **(A-A')**, *lrrk*$^{-/-}$ mutants **(B-B')** and *lrrk*$^{-/-}$ mutants harboring a genomic *lrrk* rescue construct **(C-C')** and *lrrk*$^{-/-}$ mutants rescued by overexpression of human LRRK2 (under *D42-Gal4* control) **(D-D')** expressing Lamp^{GFP} under control of the *D42-Gal4* driver. **(E)** Quantification of Lamp^{GFP} fluorescence intensities per bouton area and statistical analysis with 1-way ANOVA Kruskal-Wallis followed by Post Hoc test Dunn's multiple comparisons ****$p < 0.0001$, n >11. Individual data points are shown and the mean ± SEM is indicated.

(**F-H**) Imaging of control (*TrpA1*, **F,F'**) and *lrrk* mutant (*TrpA1, lrrk*$^{-/-}$, **G,G'**) synaptic boutons expressing temperature sensitive TrpA1 channel under control of *D42-Gal4* and Lamp^{GFP} either kept at 20°C **(F,G)** or raised to 30°C for 30 min **(F', G')**. Quantification of the Lamp^{GFP} fluorescence intensities **(H)** induced by TrpA1-dependent neuronal stimulation (at 30°C) in the indicated genotypes and statistical analysis with 1-way ANOVA Kruskal-Wallis followed by Post Hoc test Dunn's multiple comparisons ***$p < 0.0001$, n >15 image fields per genotype. Individual data points are shown and the mean ± SEM is indicated. Note that *lrrk* mutants block induction of the autophagic markers.

(**I-K**) Live imaging of NMJ boutons of animals that express Lamp^{GFP} under the control of the *D42-Gal4* driver in fed **(I,J)** and 4 h-starved **(I',J')** conditions and also over expressing the kinase-active LRRK2^{G2019S} **(I-I')** or the kinase-dead LRRK2^{D2017A} under control of D42-Gal4 **(J-J')** in a wild type background. Quantification of

Lamp^{GFP} fluorescence intensities **(K)** of the indicated genotypes and statistical analysis with 1-way ANOVA followed by a post hoc Tukey test ***p =0.0003, ****p <0.0001, n >12 image fields per genotype. Individual data points are shown and the mean ± SEM is indicated. Fluorescence intensities are shown using the scale indicated in Figure 1. Scale bars 5 µm.

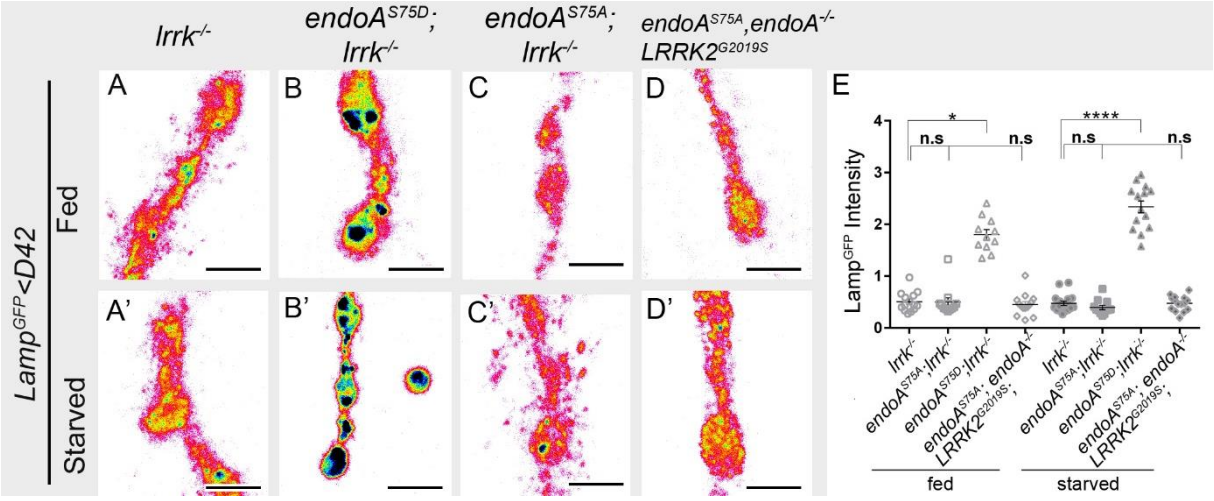

Figure S6: LRRK acts upstream of EndoA in autophagy, related to Figure 7

(A-D') Live imaging of fed **(A-D)** and 4 h-starved **(A'-D')** NMJ boutons of *lrrk*$^{-/-}$ mutants **(A-A')**, *lrrk*$^{-/-}$ mutants expressing at endogenous levels *endoA*^{S75D} **(B-B')** or *endoA*^{S75A} **(C-C')** as well as Lamp^{GFP} under control of *D42-Gal4*; and live imaging *endoA*$^{-/-}$ null mutants expressing *endoA*^{S75A} at endogenous levels and LRRK2^{G2019S} **(D, D')** as well as Lamp^{GFP} under control of the *D42-Gal4* driver. Quantification of Lamp^{GFP} fluorescence intensities **(E)** of the indicated genotypes and statistical analysis with 1-way ANOVA-Kruskal-Wallis followed by post hoc test Dunn's multiple comparisons *p = 0.0148, ****p <0.0001, n >12 image fields per genotype. Individual data points are shown and the mean ± SEM is indicated. Fluorescence intensities are shown using the scale indicated in Figure 1. Scale bar 5 µm.

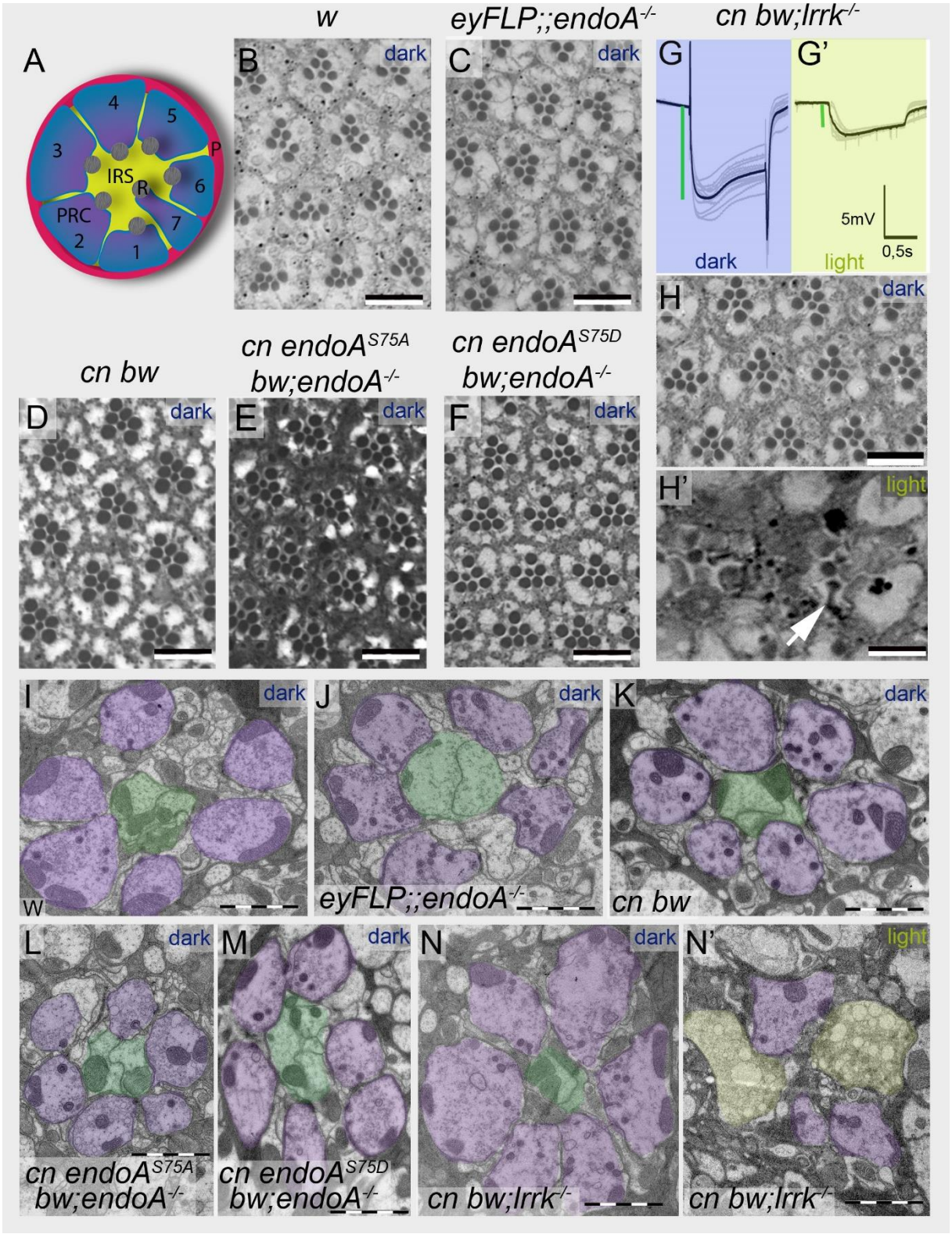

Figure S7. Neurodegeneration in *endoA* mutants, related to Figure 8

(A) Schematic drawing of *Drosophila* compound eye in a cross section shows one single eye (ommatidia) with seven photoreceptor cells (blue) and the rhabdomers (R, grey). The photoreceptors are oriented towards the inter-rhabdomeral space (IRS) and surrounded by secondary pigment cells (P, magenta).

(B-F) Histological cross sections of retinas of *w* control flies **(B)**, of flies with mutant *endoA*$^{-/-}$ eyes **(C)**, of *cn bw* control flies **(D),** of flies expressing phosphodead EndoA: *cn endoA*^{S75A} *bw; endoA*$^{-/-}$ **(E)** and phosphomimic EndoA *cn endoA*^{S75D} *bw; endoA*$^{-/-}$ **(F)**, all kept for 7 days in constant darkness, indicating no degeneration or developmental defects under these conditions.

(G-H') ERGs (depolarization upon a light flash) indicated by the green bar **(G, G')** and histological cross sections of retinas of *cn bw; lrrk*$^{-/-}$ mutants **(H, H')** of flies kept for 7 days in constant darkness **(G, H)** and of flies exposed to constant light for 3 days **(G', H')** indicating photoreceptor degeneration in *lrrk*$^{-/-}$ mutants.

(I-N) Electron micrographs of cartridges of the photoreceptor terminals in the lamina after 7 days in darkness **(I-N)** or 7 days of continuous light **(N')** of the same genotypes as in **(B-H')**. Photoreceptor terminals are marked in violet, postsynaptic neurons in green **(I-N')** and photoreceptor terminals in *lrrk* mutants reared for 7 days in light showing signs of degeneration in yellow **(N')**. A normal wild type cartridge shows 6 photoreceptor terminals **(I, J)**. Scale bars 2 µm

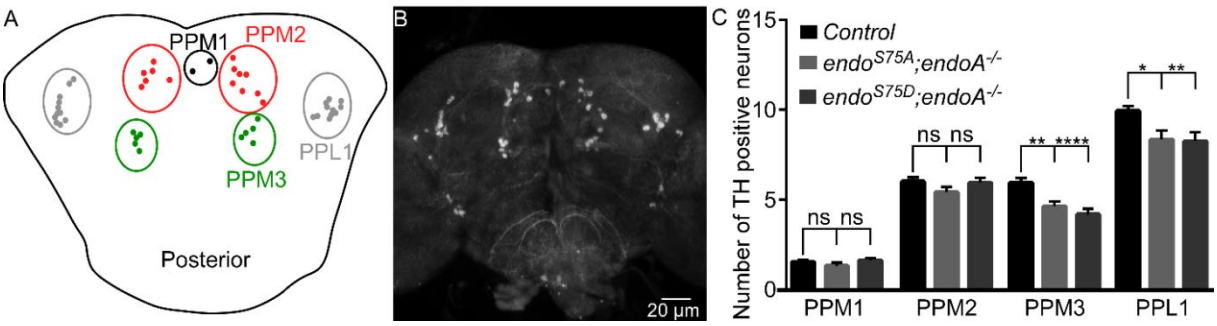

Figure S8. Balance in EndoA phosphorylation is critical for dopaminergic neuronal survival, related to Figure 8

(A) Schematic representation of TH positive clusters on posterior side of the adult fly brain. **(B)** Representative image of anti-TH staining at the posterior side of a 30-day old fly brain. **(C)** Graph showing the number of TH positive neurons in each cluster in 30 day old flies of the indicated genotypes. In 1 day old flies the number of TH positive neurons in the indicated genotypes is not different (data not shown). Statistical analysis per dopaminergic cluster with 1-way ANOVA-Kruskal Wallis test followed by a post hoc Dunn's test (bar graph with SEM indicated), n > 15 brains per genotype.

SUPPLEMENTAL EXPERIMENTAL PROCEDURES

Fly Stocks and genetics.

Flies were grown on standard cornmeal and molasses medium supplemented with yeast paste at 25°C. The following *Drosophila* stocks were obtained from the Bloomington Stock Center: *w*; P{w[+mW.hs]=GawB}D42, eyFLP;; FRT82B* w^+ *cl3R3/TM3, w1118; P{w[+mC]=UAS-mito-HA-GFP},e , P{w[+mW.hs]=GAL4-da.G32}2; MKRS/TM6B, Tb w[*]; P{w[+mC]=ple-GAL4.F}3* (also called TH-Gal4), w *and w* P[UAS-TrpA1(B (B).K}attP2. M{UAS-Atg3.ORF.3xHA.GW}ZH-86Fb* was obtained from FlyORF Stock Center. *w1118; P{GD12064}v22455* (also called UAS-RNAi-Atg3) was obtaind from VDRC Stock Center. The following fly stocks were obtained from the lab were the stock was first described:

w;;* $Lrrk^{P1e03680}$ (Lee et al., 2007), *w;* $endoA^{\Delta 4}$ (Verstreken et al., 2002), *w;* $endoA^{26}$ (Guichet et al., 2002), *transgenes expressing wild-type endoA,* $endoA^{S75A}$, $endoA^{S75D}$, human *UAS-LRRK2-V5 (*$LRRK2^{WT}$*), UAS-*$LRRK2^{KD}$*-V5 (*$LRRK2^{D2017A}$*),* $UAS\text{-}LRRK2^{G2019S}$*-V5* (Matta et al., 2012), *w; P[w{+}UAS-Atg8-mCherry* (Juhász et al., 2008), *w; P{w[+]UAS-GFP-Lamp}/CyO;TM6B/Sb* bos^1 (Pulipparacharuvil et al., 2005), *genomic w;;*$Atg8^{3xmCherry}$ (G.Juhász, unpublished) and $UAS\text{-}endoA^{4C}$ (Kasprowicz et al., 2014).

Genotypes.

The following genotypes were used:

w;UAS-mCherry::Atg8/UAS-LRRK2^{G2019S}*::V5;D42-GAL4 /+*

w;UAS-mCherry::Atg8;$lrrk^{P1}/lrrk^{P1}$*,D42-GAL4-GAL4*

w;UAS-mCherry::Atg8/$endoA^{S75D}$*;*$lrrk^{P1}/lrrk^{P1}$*,D42-GAL4*

w;UAS-mCherry::Atg8/$endoA^{S75A}$*;*$lrrk^{P1}/lrrk^{P1}$*,D42-GAL4*

w;UAS-mCherry::Atg8/$endoA^{S75A}$*;*$endoA^{\Delta 4}$*,D42-GAL4/*$endoA^{26}$

w;UAS-mCherry::Atg8/$endoA^{S75D}$*;*$endoA^{\Delta 4}$*,D42-GAL4/*$endoA^{26}$

w;$LRRK^{Bac}$*/UAS-mCherry::Atg8;*$lrrk^{P1}/lrrk^{P1}$*,D42-GAL4*

w;UAS-GFP::Lamp1;$lrrk^{P1}/lrrk^{P1}$*,D42-GAL4*

w;UAS-GFP::Lamp1/$endoA^{S75D}$*;* $endoA^{26}$*/* $endoA^{\Delta 4}$*,D42-GAL4*

w;UAS-GFP::Lamp1/$endoA^{S75A}$*;*$endoA^{26}$*/* $endoA^{\Delta 4}$*,D42-GAL4*

w;$LRRK^{Bac}$ *UAS-GFP::Lamp1;*$lrrk^{P1}/lrrk^{P1}$*,D42-GAL4*

w;UAS-mCherry::Atg8/UAS-LRRK2::V5; $lrrk^{P1}/lrrk^{P1}$*,D42-GAL4*

w;UAS- GFP::Lamp1/UAS-LRRK2::V5; $lrrk^{P1}/lrrk^{P1}$*,D42-GAL4*

w;UAS-GFP::Lamp1/UAS-LRRK2^{D2017A}::V5;D42-GAL4/+

w;UAS-GFP::Lamp1/UAS-LRRK2^{G2019S}::V5;D42-GAL4/+

w;UAS-mCherry::Atg8/UAS-LRRK2^{D2017A}::V5;D42-GAL4/+

w;endoA^{S75D}/UAS-GFP::Lamp1;lrrk^{P1}/lrrk^{P1},D42-GAL4

w;endoA^{S75A}/UAS-GFP::Lamp1;lrrk^{P1}/lrrk^{P1},D42-GAL4

w;UAS-Lamp::GFP/+;D42-GAL4/+

w;endoA^{S75A},cn,bw; endoA$^{\Delta 4}$/endoA^{26}

w;endo^{S75D},cn,bw; endoA$^{\Delta 4}$/ endoA^{26}

y,w,eyFLP/w;FRT 82B,endoA^{delta4}

w;UAS-GFP::Atg9/D42-GAL4

w;UAS-GFP::Lamp1;D42-GAL4/UAS-TrpA1

w;UAS-GFP::Lamp1;lrrk^{P1},D42-GAL4/UAS-TrpA1, lrrk^{P1}

w;UAS- mCherry::Atg8;D42-GAL4/UAS-TrpA1

w;UAS- mCherry::Atg8;lrrk^{P1},D42-GAL4/UAS-TrpA1, lrrk^{P1}

w;cn,bw;lrrk^{P1}

w;UAS-mCherry::Atg8;UAS-GFP::Atg9,D42-GAL4/D42-GAL4

w;endoA^{WT}/UAS-mCherry::Atg8;endoA^{26}/endoA$^{\Delta 4}$,D42-GAL4

w;UAS-GFP::Lamp1/endoA^{WT};endoA^{26}/endoA$^{\Delta 4}$,D42-GAL4

w;endoA^{S75A}/UAS-mCherry::Atg8;UAS-LRRK2^{G2019S}::V5,endoA^{26}/endoA$^{\Delta 4}$,D42-GAL4

w;UAS-mCherry::Atg8/endoA^{4C};endoA$^{\Delta 4}$,D42-GAL4/+

w;UAS-LRRK2^{G2019S}::V5/+;Da-Gal4 /+

w;UAS-LRRK2^{G2019S}::V5/+;Da-Gal4/UAS-GFP::Atg9

w;UAS-mCherry::Atg8/+;UAS- Atg3::HA/D42-GAL4

w;UAS-mCherry::Atg8/endoA^{S75D};endoA$^{\Delta 4}$,D42-GAL4/ UAS- Atg3::HA, endoA^{26}

w;UAS-mCherry::Atg8/endoA^{S75A};endoA$^{\Delta 4}$,D42-GAL4/ UAS- Atg3::HA, endoA^{26}

w;UAS-mCherry::Atg8/+;D42-GAL4 /+

shi^{ts1};UAS-mCherry::Atg8/+;D42-GAL4 /+

w;endoA^{S75A}/+;endoA$^{\Delta 4}$,D42-GAL4/endoA^{26} ,UAS-GFP::Atg9

w;endoA^{S75D}/+;endoA$^{\Delta 4}$,D42-GAL4/endoA^{26} ,UAS-GFP::Atg9

genomic w;;Atg8^{3xmCherry}

w;UAS-mCherry::Atg8/+;D42- GAL4, UAS-Mito^{GFP}/+

w;;TH-Gal4/+

w; endoA^{S75A};endoA^{26}/ endoA$^{\Delta 4}$

w; endoA^{S75D};endoA^{26}/ endoA$^{\Delta 4}$

w;;D42-GAL4/+

w;UAS-GFP::Atg9/D42-GAL4

w;UAS- Atg3::HA /D42-GAL4

w;UAS-RNAi-Atg3/+;D42-GAL4/+

Primers.

-UAS-GFP::Atg9: GFP-FW primer aac aga tct gcg gcc gcg gcc aaa atg gtg agc aag ggc gag gag, GFP-RC primer ttg ata tgt ggg cta gac atc ttg tac agc tcg tcc atg c, Atg9-FW primer gca tgg acg agc tgt aca aga tgt cta gcc cac ata tca a, Atg9-RC primer cct tca caa aga tcc tct agt tag atc cac tct ggc cgc t.

-pFN18a EndoA: endoA_FW_ pFN18a TCAGGCGATCGCCATGGCTTTCGCCGGACTCAAAAAGCAG endoA_Rev_ pFN18a ATGCGTTTAAACGTTGCCATTGGGCAGGGGCAC

-pFN18a Atg3::mCherry-Myc: Atg3::mCherry-Myc: Fw_ pFN18a_atg3 CTTTCAGAGCGATAACGCGATCGCCATGCAGAGTGTTCTCAACAC, Rev_linker_atg3 GCCACCTCCGCCTCCACCAGACATGTTGAAGTTTTGCGT, Fw_linker_mCherry GGTGGAGGCGGAGGTGGCatggtgagcaagggcgaggag, Rev_ pFN18a _myc CCGGGTACCGAGCCCGAATTCGTTTAAACTTACAGATCCTCTTCTGAGA

Protein expression and purification

Full-length cDNA *Drosophila* endoA^{WT}, endoA^{S75A}, endoA^{S75D} were amplified by PCR and cloned into pFN18a Flexi Vector (Promega). *Drosophila* Atg3:: mCherry-Myc was created by Gibson assembly (NEB) using two PCR products encompassing Atg3 and mCherry-Myc and cloned into pFN18a Flexi Vector (Promega). The N-terminal Halo-tagged proteins were expressed in *E. coli* KRX strain and purified using Halo linked resin followed by Tev cleavage and subsequent purification with His-linked beads.

Immunoprecipitation (IP).

Adult flies with the following genotype were frozen on dry ice w;*UAS-LRRK2^{G2019S}::V5/+;Da-Gal4* and w;*UAS-LRRK2^{G2019S}::V5/+;Da-Gal4/UAS-GFP::Atg9* and decapitated by vigorously vortexing. Heads were separated from the body by sieving. Heads were homogenized on ice using a French press, in 2 ml of homogenization buffer containing 300mM sucrose, 4mM HEPES (pH7.4), protease inhibitor complete and Phospho-Stop (Roche). The homogenate was cleared from debris by centrifugation for 10 min at 1000 x g. 150 µl of the supernatant was loaded onto 25 µl of GFP-Trap _M beads (Chromotec) and incubated for 1 hour at 4°C on a shaker. GFP-Trap was magnetically separated and washed twice with 10 mM Tris pH7.5, 150 mM NaCl 0.5 mM EDTA. For the gel analysis, beads were resuspended in 30 µl PBS and 10 µl 4xSDS buffer, denatured for 15 min at 75°C and separated by SDS-PAGE. For Western blots, SDS-PAGE gels were blotted onto PDVF transfer membrane (Millipore) and incubated with antibodies using standard procedures. Antibody dilutions used: α-GFP (A-11122) (Invitrogen)1:2000, anti-EndoA (GP69) 1:5000 (Verstreken et al., 2002), peroxidase-conjugated secondary antibodies 1:1000. The ECL system (Perkin Elmer) was used for detection and chemiluminescence was imaged using LAS-3000 (Fuji Film).

Electroretinograms (ERGs).

Flies were immobilized with liquid Pritt glue, and a glass recording electrode filled with 3 N NaCl was placed on the eye, whereas the reference electrode filled with 3 N NaCl was placed in the thorax of the fly. 1 s light pulses were delivered using a digitally controlled white light-emitting diode. The depolarization amplitude was measured by determining the minimum amplitude between time point 538 ms and 1200 ms of the 2 s ERG recording. Data were recorded with Clampex 10.2 (Molecular Devices). Raw data traces and average traces were analyzed in Clampfit 10.3 2 (Molecular Devices) and Igor Pro (WaveMetrics).

Light induced degeneration and histology

Light-induced retinal degeneration was assessed by placing flies for 2, 3 or 7 days in continuous illumination at 1300-lux and 25 °C (Soukup et al., 2013). Histological (2.5 µm) sections of the retina were then prepared as followed: fly heads were bisected, fixed in 2% paraformaldehyde and 2% glutaraldehyde in 0.1 M Na-Cacodylate buffer (pH 7.4) for 2 h at room temperature and washed in 0.1 M phosphate buffer (pH 7.4), followed by simultaneous fixation in 1% osmium tetroxide/2% glutaraldehyde, followed by 2% OsO4. After dehydration, eyes were embedded in Araldite and semi-thin (2.5 µm) sections were cut on a microtome and

stained with toluidine blue. Histological sections were analyzed by conventional light microscopy using the Leica DMRXA.

Electron microscopy

Correlative light and electron microscopic studies (CLEM) using Near-infrared branding (NIRB) were performed as described previously (Bishop et al., 2011; Urwyler et al., 2015). Larvae were starved for 3-4 hours, dissected in HL3 and fixed (0.5% glutaraldehyde, 2% paraformaldehyde in 0.1 M Phosphate buffer, pH= 7.2) for 2 hours at room temperature in the dark, followed by washing steps in 0.1 M Phosphate buffer, pH= 7.2. The bleaching function of the ZEN2010 software (Zeiss) was used to perform NIRB on a LSM 710 upright confocal microscope as described by Urwyler et al., (2015). Branding marks were introduced to the tissue with a Mai Tai DeepSee two-photon laser (Spectra-Physics) at 880 nm and 95% maximal power output. Z-stacks of the region of interest were acquired before and after NIRB. Processed larvae were post-fixed in 1% glutaraldehyde, 2% paraformaldehyde in 0.1 M Phosphate buffer, pH= 7.2 at 4ºC over night or until further processing. Specimen were processed for TEM as described previously (Fernandes et al., 2014). Essentially, samples were osmicated for 2 hours in 2% OsO_4/Phosphate buffer and subsequently stained 1.5 hours in 2% aqueous uranyl acetate. Specimen were dehydrated in an ascending series of ethanol solutions and embedded in Agar 100 (Laborimpex; Agar Scientific). Ultrathin sections (100 nm) of the region of interest were cut with an ultramicrotome (EM UC7; Leica), collected on one-slot grids (EMS), post-stained in 2% aqueous uranyl acetate (4 min) and Reynolds lead citrate (2 min) and imaged on a JEM 1400 transmission electron microscope (JEOL) at 80 kV with a bottom mounted camera (Quemasa; 11 megapixels; Olympus) running iTEM 5.2 software (Olympus). Branding marks introduced by NIRB were used to identify *Drosophila* NMJ boutons previously imaged on the confocal microscope. Overlay of electron and fluorescent micrographs, identification of $Atg8^{mCherry}$ positive ultrastructural features and processing of micrographs using brightness and contrast were performed with ImageJ and Adobe Photoshop Elements 14.

Transmission electron microscopy of adult eyes was performed as described previously in (Slabbaert et al., 2016). Heads from adult flies were removed from the body, cut in half and immediately fixed in 2% paraformaldehyde and 2% glutaraldehyde in 0.1 M Na-Cacodylate buffer (pH 7.4) for 2 h at room temperature. After overnight fixation at 4 °C, samples were washed with 0.1 M Na-Cacodylate, pH 7.4, and subsequently osmicated with 2% osmium (OsO4/Na-Cacodylate buffer). After dehydration in an ascending series of ethanol solutions and staining in 4% aqueous uranyl acetate solution the specimen were embedded in Agar 100

(Laborimpex; Agar Scientific). Ultrathin sections (70 nm) of the retina and the lamina were collected on grids (Laborimpex; Agar Scientific) coated with Butvar and imaged at a 5kx zoom as described above.

Immunohistochemistry.

Immunohistochemistry of third instar larval NMJs was performed by dissecting larvae in HL3 on sylgard plates and then fixing with paraformaldehyde 4 % in HL3 for 20 min. After 45 min permeabilisation with 0.4 % triton in PBS larvae of different genotypes were physically marked and treated in the same tube for labeling. Samples were preblocked with 10 % NGS-PBT (0.4 % Triton in PBS) for 30-60 min and then incubated with primary antibodies overnight at 4°C. Samples were washed several times and then incubated with secondary antibodies in PBT with 10 % NGS for 2 h at room temperature. The samples were finally mounted in Vectashield (Vector Laboratories).

The following antibodies were used to stain third instar *Drosophila* larvae and adult brains: rat α-HA[1:1000 (Roche; Clone 3F10,)]; mouse α-HA[1:3000 (Covance; Clone 16B12)], chicken α-GFP [1:1000 (Invitrogen; A10262)], rabbit α-GFP [1:100 (Invitrogen; A-11122)], guinea pig α-endoA (GP69) [1:1000 (Verstreken 2002)], chicken α-mCherry [1:1000 (Novus; NBP2-25158)], mouse α-Dlg [(1:500) DSHB; 4F3], rabbit α-drosophila Lamp1 [(1:1000) gift from Tor Erik Rusten]. Pacific Blue-, Alexa Fluor 488-/Alexa Fluor 555-conjugated secondary antibodies: 1:1000 and Alexa Fluor 647-conjugated antibodies at 1:400 (Invitrogen). Fixed samples were imaged on a Nikon A1R confocal microscope through a 60X NA1.2 water immersion lens.

FlAsH FALI

Larvae were dissected in HL3, incubated in 1 μM FlAsH for 10 min in the dark and washed first in Bal buffer (Invitrogen) and then several times in HL3. One hemisegment was subsequently illumined through a 40x 0.8NA water immersion objective on a Nikon eclipse F1 microscope using epifluorescent 500±12 nm (Intensilight C-HGFI; Nikon) band pass-filtered light (ex:500/24; dichroic mirror, 520) for 5 min. Motor nerves were then stimulated as indicated in the **'**Induction of autophagy and flux assay' section and $Atg8^{mCherry}$ was imaged.

GUV imaging.

GUVs for Atg3 binding assay were imaged on a Nikon A1R confocal microscope through a 60X NA1.2 water immersion lens. Single confocal planes of GUVs were scanned using identical settings.

GUVs for the EndoA tubulation assay were imaged using the IN Cell Analyzer 2000 inverted microscope (GE Healthcare) and a Roper scientific CoolSNAP K4 high performance large chip (4.2Mp) CCD camera operated by the IN Cell software. Images were acquired with a FITC 490/20 band pass excitation filter and a FITC 525/36 band pass emission filter.

Quantitative real time PCR

Total RNA was extracted from 5-6 control larvae (*cs^{w}/+;;D42-GAL4/+*), larvae either over-expressing ATG8^{mCherry} (*cs^{w}/+; UAS ATG8^{mCherry}/+;D42-GAL4/+*), ATG3^{HA} (*cs^{w}/+; UAS ATG3^{HA}/D42-GAL4*) or ATG9^{GFP} (*cs^{w}/+; UAS ATG9^{GFP}, D42-GAL4/+)* in motor neurons using the *D42-GAL4* driver and from larvae expressing a genomic ATG8^{3xmCherry} transgene (*ATG8^{3xmCherry}/D42-GAL4, UAS mito-GFP*) using the ReliaPrep™ miRNA Cell and Tissue Miniprep System (Promega). The manufacturer's protocol was followed including a DNAseI treatment to prevent DNA contamination. Subsequently, cDNA was amplified from 1 µg of RNA using the SuperScript ® III First-Strand Synthesis System for RT-PCR (Life Technologies) using a mix of oligo(dt) primers and random hexamer primers. A mock control without reverse transcriptase was included for all samples. Next, 5 µl of 4 ng/µl cDNA, mock or water (no template control) were loaded together with 6 µM of the forward and reverse primers for ATG8, ATG3 or ATG9 and the LightCycler® 480 SYBR Green I Master mix (Roche). Subsequently, the LightCycler 480 was used for analysis (Roche). Used primers primers (designed using FlyPrimerBank (Hu et al., 2013) are listed below.The ribosomal protein RP49 was used as house-keeping gene to normalize the data for loading differences. Primers were selected by their amplification efficiency that was determined for each amplicon based on dilution series (1–1:256). Finally, the fold change of mRNA expression was determined for each gene using the Δ-Δ-CT method, where the expression of the transgenes was compared to the control sample.

ATG8a_FP2	CCCTGTACCAGGAACATCACG
ATG8a_RP2	GGCCATGCCGTAAACATTCTC
ATG3_FP1	CCAAGACAAAACCCTACCTACC
ATG3_RP1	GCCGACGTATTCCATCTGCT
ATG9_FP1	ACACGCCTCGAAACAGTGG
ATG9_RP1	TCAAGGTCCTCGATGTGGTTC

RP-49_F	ATCGGTTACGGATCGAACAA
RP-49_R	GACAATCTCCTTGCGCTTCT

Visualization of dopaminergic clusters after aging adult flies

1-3 day old adult flies were kept on rich molasses and corn food medium for 30 days at 25°C. Every 3 days the food vial was replaced to prevent flies sticking to the food. At day 30, fly brains were dissected in ice-cold PBS and fixed with 3,7% formaldehyde in PBST (PBS + 0.1% Triton X-100) for 20 minutes. Subsequently, the brains were washed for 1 h in PBST and blocked for 1h with 5 % BSA in PBST. After overnight incubation with the rabbit anti-TH antibody (1:300, Millipore) at 4°C in 5 % BSA in PBST, samples were washed with PBST for 1 h. Subsequently, the Alexa 488 secondary antibody (1:500, Life Technologies) was incubated for 1,5 h in 5% BSA in PBST. After 1 h washing with PBST, brains were mounted in Vectashield (Vector Laboratories). The dopaminergic clusters (labeled by the anti-TH antibody) were imaged using a 20x objective 0.75 NA (Nikon) and a Nikon A1R confocal microscope. The total number of dopaminergic neurons for the PPM1, PPM2, PPM3 and PPL1 clusters were counted manually throughout the brain and in both hemispheres.

SUPPLEMENTRAY REFERENCES

Bishop, D., Nikic, I., Brinkoetter, M., Knecht, S., Potz, S., Kerschensteiner, M., Misgeld, T., 2011. Near-infrared branding efficiently correlates light and electron microscopy. Nat Meth 8, 568–570.

Fernandes, A.C., Uytterhoeven, V., Kuenen, S., Wang, Y.-C., Slabbaert, J.R., Swerts, J., Kasprowicz, J., Aerts, S., Verstreken, P., 2014. Reduced synaptic vesicle protein degradation at lysosomes curbs TBC1D24/sky-induced neurodegeneration. J. Cell Biol. 207, 453–62.

Guichet, A., Wucherpfennig, T., Dudu, V., Etter, S., Wilsch-Bräuniger, M., Hellwig, A., González-Gaitán, M., Huttner, W.B., Schmidt, A. a, 2002. Essential role of endophilin A in synaptic vesicle budding at the Drosophila neuromuscular junction. EMBO J. 21, 1661–72.

Hu, Y., Sopko, R., Foos, M., Kelley, C., Flockhart, I., Ammeux, N., Wang, X., Perkins, L., Perrimon, N., Mohr, S.E., 2013. FlyPrimerBank: an online database for Drosophila melanogaster gene expression analysis and knockdown evaluation of RNAi reagents. G3 (Bethesda). 3, 1607–16.

Juhász, G., Hill, J.H., Yan, Y., Sass, M., Baehrecke, E.H., Backer, J.M., Neufeld, T.P., 2008. The class III PI(3)K Vps34 promotes autophagy and endocytosis but not TOR signaling in Drosophila. J. Cell Biol. 181, 655–66.

Kasprowicz, J., Kuenen, S., Swerts, J., Miskiewicz, K., Verstreken, P., 2014. Dynamin photoinactivation blocks Clathrin and α-adaptin recruitment and induces bulk membrane retrieval. J. Cell Biol. 204 , 1141–1156.

Lee, S.B., Kim, W., Lee, S., Chung, J., 2007. Loss of LRRK2/PARK8 induces degeneration of dopaminergic neurons in Drosophila. Biochem. Biophys. Res. Commun. 358, 534–539.

Matta, S., Van Kolen, K., da Cunha, R., van den Bogaart, G., Mandemakers, W., Miskiewicz, K., De Bock, P.-J., Morais, V. a, Vilain, S., Haddad, D., Delbroek, L., Swerts, J., Chávez-Gutiérrez, L., Esposito, G., Daneels, G., Karran, E., Holt, M., Gevaert, K., Moechars, D.W., De Strooper, B., Verstreken, P., 2012. LRRK2 controls an EndoA phosphorylation cycle in synaptic endocytosis. Neuron 75, 1008–21.

Pulipparacharuvil, S., Akbar, M.A., Ray, S., Sevrioukov, E. a, Haberman, A.S., Rohrer, J., Krämer, H., 2005. Drosophila Vps16A is required for trafficking to lysosomes and biogenesis of pigment granules. J. Cell Sci. 118, 3663–3673.

Slabbaert, J.R., Kuenen, S., Swerts, J., Maes, I., Uytterhoeven, V., Kasprowicz, J., Fernandes, A.C., Blust, R., Verstreken, P., 2016. Shawn, the Drosophila Homolog of SLC25A39/40, Is a Mitochondrial Carrier That Promotes Neuronal Survival. J. Neurosci. 36, 1914–1929.

Soukup, S.F., Pocha, S.M., Yuan, M., Knust, E., 2013. DLin-7 is required in postsynaptic lamina neurons to prevent light-induced photoreceptor degeneration in drosophila. Curr. Biol. 23, 1349–1354.

Urwyler, O., Izadifar, A., Dascenco, D., Petrovic, M., He, H., Ayaz, D., Kremer, A., Lippens, S., Baatsen, P., Guerin, C.J., Schmucker, D., 2015. Investigating CNS synaptogenesis at single-synapse resolution by combining reverse genetics with correlative light and electron microscopy. Development 142, 394–405.

Verstreken, P., Kjaerulff, O., Lloyd, T.E., Atkinson, R., Zhou, Y., Meinertzhagen, I. a., Bellen, H.J., 2002. Endophilin Mutations Block Clathrin-Mediated Endocytosis but Not Neurotransmitter Release. Cell 109, 101–112.